AD-A136 589 ALLOY DEVELOPMENT PROCESSING AND CHARACTERIZATION OF DEVITRIFIED TITANIUM. (U) NORTHEASTERN UNIV BOSTON MA BARNETT INST OF CHEMICAL ANALYSIS.. S H WHANG DEC 83 1/1

UNCLASSIFIED N00014-82-K-0597 F/G 11/6 NL

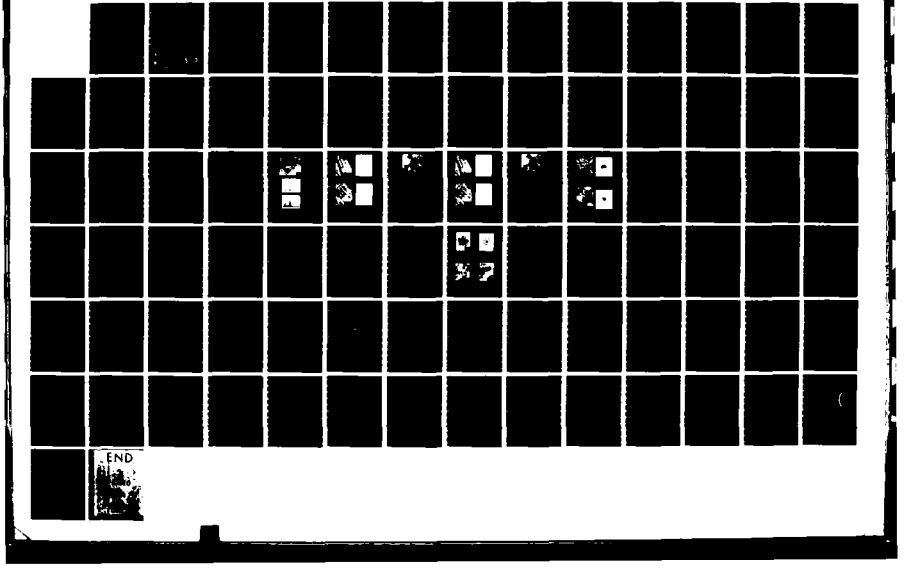

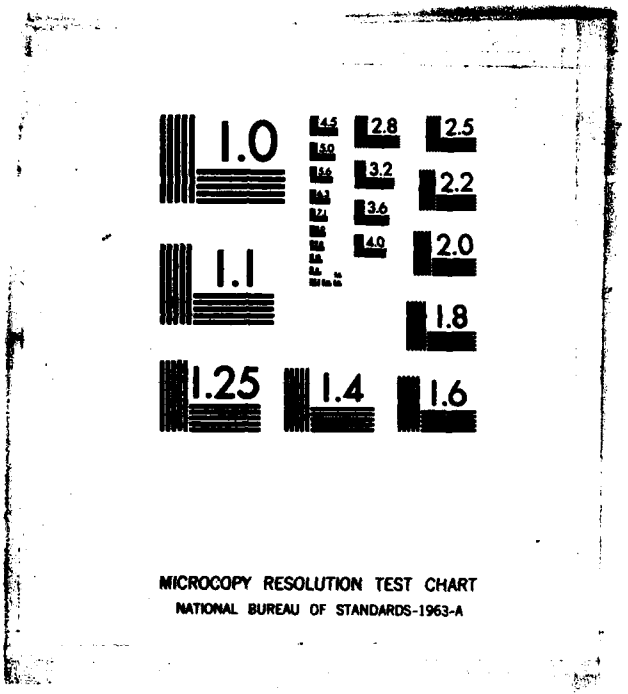

(12)

CHARACTERIZATION
MICROCRYSTALLINE ALLOYS

Science

SECURITY CLASSIFICATION OF THIS PAGE (When Data Entered)

REPORT DOCUMENTATION PAGE		READ INSTRUCTIONS BEFORE COMPLETING FORM
1. REPORT NUMBER	2. GOVT ACCESSION NO. AD-A136589	3. RECIPIENT'S CATALOG NUMBER
4. TITLE (and Subtitle) ALLOY DEVELOPMENT, PROCESSING AND CHARACTERIZATION OF DEVITRIFIED TITANIUM BASE MICROCRYSTALLINE ALLOYS		5. TYPE OF REPORT & PERIOD COVERED Annual Report September 1982-August 1983
		6. PERFORMING ORG. REPORT NUMBER
7. AUTHOR(s) S. H. Whang		8. CONTRACT OR GRANT NUMBER(s) N00014-82-K-0597
9. PERFORMING ORGANIZATION NAME AND ADDRESS 341 Mugar, Northeastern University Barnett Institute of Chem. Anal. & Mat. Science Boston, MA 02115		10. PROGRAM ELEMENT, PROJECT, TASK AREA & WORK UNIT NUMBERS
11. CONTROLLING OFFICE NAME AND ADDRESS Office of Naval Research 800 N. Quincy St. Arlington, VA 22217		12. REPORT DATE December 1983
		13. NUMBER OF PAGES 88
14. MONITORING AGENCY NAME & ADDRESS(if different from Controlling Office)		15. SECURITY CLASS. (of this report) Unclassified
		15a. DECLASSIFICATION/DOWNGRADING SCHEDULE

16. DISTRIBUTION STATEMENT (of this Report)

This document has been approved for public release and its distribution is unlimited. Reproduction in whole or in part is permitted by the U.S. Government.

17. DISTRIBUTION STATEMENT (of the abstract entered in Block 20, if different from Report)

18. SUPPLEMENTARY NOTES

19. KEY WORDS (Continue on reverse side if necessary and identify by block number)

Devitrified Ti alloy, rapidly solidified microcrystalline alloy, arc plasma melt spinning process, microstructural & mechanical properties of rapidly solidified Ti alloys, rare earth precipitate, metalloid precipitate, age hardened Ti alloy, precipitate coarsening.

20. ABSTRACT (Continue on reverse side if necessary and identify by block number)

New syntheses of devitrified Ti alloys as well as rapidly solidified microcrystalline Ti alloys have been made using novel additive elements (B, Si, Y, La Ce, etc.) and rapid quenching techniques. The glass forming property of binary and ternary alloy systems has been studied using a model based on a phenomenological approach. The extended solid solubility of the additives were determined by TEM.

The microstructures of the DV as well as RS microcrystalline alloys have been investigated by AEM with respect to heat treatment conditions. The

DD FORM 1 JAN 73 1473

Unclassified

SECURITY CLASSIFICATION OF THIS PAGE (When Data Entered)

DEPARTMENT OF DEFENSE FORMS

. DD Form 1473: Report Documentation Page

SECURITY CLASSIFICATION OF THIS PAGE(When Data Entered)

crystal structure, morphology and coarsening kinetics of the precipitate resulting from the heat treatment in the synthesized alloys have been studied by TEM, SEM, STEM, x-ray, EDXS and ELS. Mechanical properties such as microhardness and bend ductility were measured on the samples heat treated isothermally as well as isochronally. From the results, microstructure-mechanical property relationships have been found.

Unclassified

SECURITY CLASSIFICATION OF THIS PAGE(When Data Entered)

ABSTRACT

New syntheses of devitrified Ti alloys as well as rapidly solidified microcrystalline Ti alloys have been made using novel additive elements (B, Si, Y, La, Ce, etc.) and rapid quenching techniques. The glass forming property of binary and ternary alloy systems has been studied using a model based on a phenomenological approach. The extended solid solubility of the additives were determined by TEM.

The microstructures of the DV as well as RS microcrystalline alloys have been investigated by AEM with respect to heat treatment conditions. The crystal structure, morphology and coarsening kinetics of the precipitate resulting from the heat treatment in the synthesized alloys have been studied by TEM, SEM, STEM, x-ray, EDXS and ELS. Mechanical properties such as microhardness and bend ductility were measured on the samples heat treated isothermally as well as isochronally. From the results, microstructure-mechanical property relationships have been found.

TABLE OF CONTENTS

STATEMENT OF PROBLEMS STUDIED

The research conducted during the first year is comprised largely of two categories:

1. To study principles for the alloy syntheses through rapid solidification processing. The study includes: the extended solid solubility of the novel additive elements; the identification of the crystal structure, morphology, thermal stability of the second phases originating from the additives; the effects of these second phases on age behavior, and other mechanical properties; and the overall structure-property relationship.

2. To develop the rapid solidification processing using the arc-plasma melt spinning technique. This includes the construction of a pilot arc-melt spinner which can process a few pound of a Ti alloy at a time into ribbons or flake materials and the establishment of the processing parameters for the spinning.

SUMMARY OF PRINCIPLE RESULTS

1. INTRODUCTION

For a long time, the design principles for Ti alloys have relied on solid solution strengthening mechanism with an exception for the Si containing alloys. One of the important reasons for that lies in the fact that the conventional processing methods depend heavily on the feasibility of a solution treatment. Now, rapid solidification processing provides means that can remove such a major stumbling block and pave the way for new syntheses of Ti alloys which employ precipitate as well as dispersoid strengthening mechanisms at the elevated temperature.

The establishment of the new design principles requires a series of experiments that would elucidate the supersaturation of the additives, the morphology as well as the coarsening of the precipitates and the structure-property relationships. Some achievement in these areas in the first year of RS Ti alloy program at Northeastern University is summarized as follows.

2. EXPERIMENTAL

Much attention has been paid to the experimental uncertainty associated with the preparation of specimens. There are two aspects to be considered: Firstly, to avoid a significant variation in the measurement, the sample thickness is fixed for a series of experiments since the cooling rate, which is a linear function of the thickness, governs the microstructure and thereby mechanical properties.

Secondly, for the heat treatment, the samples were wrapped with Ta foil and sealed together with additional Ti foils as getter materials in a vacuum of 10^{-3} or 10^{-4} torr. Frequently, the failure to attain a low oxygen pressure results in an oxide form of the rare earth (RE) compound

instead of other forms such as group IIIA, IVA metals-RE rich precipitates. For example, the as-quenched Ti-5Al-3La aged at 700°C,2h, under a 30 mm torr shows a significant amount of cuboidal oxide precipitate while the same alloys aged at 700°C, 2h, under a 10^{-4} torr exhibits very fine spherical precipitate which tentatively was identified as Al_4La (orthorhombic).

3. SOLUBILITY OF ADDITIVE ELEMENTS IN TITANIUM

The homogeneity of compositions as well as the refinement of microstructures are an essential part of the RS processing. In particular, the extended solubility of an insoluble additive element via rapid solidification has a beneficial aspect for the alloy design based on the second phase strengthening. To date, the additives being widely used are metalloids (Si,B) and rare earth metals (Y, La, Ce, Nd, Er, etc.). Both type additives are poor solid solution formers with Ti for different reasons. The primary reason for the poor solubility may be easily explained with the two well-known parameters, atomic size ratio between the host and solute atoms and the heat of solution. The metalloids have a very small atomic size and a very large heat of solution in Ti, which lead to compound formation between them whereas the rare earth metals have a very large atomic size and a positive heat of solution in Ti, which results in a immiscible phase.

TABLE 1

Alloy	Phase Diagram Feature	Maximum Equilibrium Solubility in Phase Diagram at % (°C)	Maximum Extended Solubility at %
Ti-Si	eutectic	5 (1330)	<6
Ti-B	eutectic	~1 (1540)	>6
Ti-C	eutectic	~1.5 (1650)	~10

Ti-La	monotectic	~1 (1550) ~1 (900)	<0.3
Ti-Ce	monotectic	~2 (1390) ~1 (900)	~0.6

* by the Hammer and Anvil technique (cooling rate $\sim 10^6$k/sec)

Table 1 shows a crude measurement of an extended solid solubility of the additives by TEM. At first, a large equilibrium solubility of metalloids results in a large extended solubility and a small equilibrium solubility of the RE metals to a small extended solubility. Also, an unusual behavior of the extended solubility in the Ti-RE systems has been observed, i.e., the maximum extended solubility is smaller than the maximum equilibrium solubility. This behavior may be understood from the monotectic phase diagram feature of the binary Ti-RE system, in which a large liquidus and solidus interval exists. Hence, it is likely that the supercooled liquid decomposes into RE rich liquid and β phase in the interval zone. This has been observed in the Ti-(2-4)La and the Ti-6Al-4V-3La systems where the RE deposits along the subgrain boundary. Also, this may be true from the viewpoint of the undercooling and nucleation from a liquid because an extremely high undercooling (>0.4 Tm) as well as homogeneous nucleation from the liquid can't be obtained using low grade materials and a large quantity of liquid alloys. In addition, in the table, the maximum extended solubility increases with decreasing the atomic size of the additive element within the same type of additives.

4. DEVITRIFIED (DV) Ti ALLOYS

The advantage of DV Ti alloy is that extremely homogeneous and fine microstructures including precipitates can be generated from a glassy

phase. However, one stringent compositional requirement is that the alloy must be transformed into a glassy phase for a given cooling rate. It has happened that some high-metalloid Fe based alloys satisfy both the glass forming requirement as well as the alloy design criteria.

In this program, the glass forming ability (GFA) of some binary and ternary alloys has been studied using a model. In addition, some multi-component DV Ti alloys have been synthesized and investigated with respect to microstructures and mechanical properties.

a) Glass Forming Property

It is well known that both the liquidus curvature near eutectic and the terminal solubility are two important factors affecting glass forming property, which has been observed from the experiments. Furthermore, a Temperature-Composition Map (T-C map) that takes into account these two factors using T_0 line as a scaling parameter has been used to predict the glass forming property of a binary or ternary alloy system, where T_0 is an intersecting point of the two loci of the liquidus and solidus curves in the free energy composition diagram. The results have been satisfactory with a certain accuracy, though it is based on a phenomenological model. In fact, it is possible that the model may predict the glass forming compositional range (GFCR) with a large error because of the non-linear nature of the T_0 line in an actual case. Another problem arises from the intermetallic phase or intermetallic compound phase whose glass forming property is not well known. It has been observed that the crystallization of a low-melting intermetallic compound can be suppressed during rapid quenching from the liquid, which allows the supercooled liquid to transform into a glassy phase. In

contrast, a very high-melting intermetallic compound can be suppressed and therefore treated as a terminal phase such as a pure component from which a T_o line originates. When a prediction of a GFA in an alloy system is made by the T-C model using a partial or a sub-phase diagram instead of using a whole phase diagram, the results for GFCR improve drastically. The sub-phase diagram consists of one terminal pure component and one neighboring intermetallic compound phase or two neighboring intermetallic compounds as two terminal phases. It is very difficult to know which compound can't be suppressed upon rapid quenching and act as a terminal phase in a sub-phase diagram since there is no theoretical or experimental basis to determine the GFA of a compound. Therefore, the glass forming property of a compound phase could be an interesting subject to be investigated in the future.

b) Glass Forming Composition in Binary and Ternary Alloy Systems

The predicted glass forming compositions for Ti-Pt, Ti-Ni and Ti-Si by the T-C model based on a sub-phase diagram are in a good agreement with those produced by the experiments. Particularly, the improvement of the prediction due to the sub-phase diagram scheme is significant for the hypereutectic compositions.

On the other hand, the T-C model also has been applied to a ternary system, Ti-Zr-Si in combination with a computer technique to calculate the phase diagram. In this system, the reference liquidus surface is constructed using the melting points of the two pure components and the two compound phases (Ti_5Si_3, Zr_5Si_3).

The predicted GFCR is also in a good agreement with the experimental GFCR. The results indicate that basically the GFA is

governed by the liquidus depression as well as the solid solubility. By and large, the pronounced liquidus depression in a ternary alloy provides a large glass forming region.

c) Syntheses of DV Ti Alloy

Many Ti glassy alloys have been made using a variety of alloying elements. In the case of the alloy syntheses, a general rule for a selection of a possible glass forming alloy composition has been established. The alloying elements largely are divided into two categories: 1) Solid solution forming elements such as Zr, Hf, V, Mo, Cr, Al, Sn, etc., to provide solid solution strengthening; 2) glass forming elements such as Fe, Co, Ni, Cu, B, Si, etc. It was found that for the cooling rate of ~10^6K/sec, a glassy Ti alloy composition is made of solid solution strengthening elements in 70-80 at % and glass forming elements in 20-30 at %, i.e.

$Ti(Zr,Hf,V,Mo---)_x$ $Si(B,Fe,Co,Ni---)_y$ where x = 70-80, y = 30-20.

The devitrification as well as the succeeding age treatment of the Ti glasses has been conducted at 550-700°C. The microstructures resulting from the devitrification are on extremely small scales. Both the grain size and the precipitate are less than 0.1 μm diameter. The resulting strength increase is as much as ~100% from that of the as-quenched state whereas the ductility decreases to an unacceptable level when excessive metalloid is used. After the high temperature annealing, the grain size remains within a submicron average. The strength at this stage still is much higher than that of the as-quenched state. Various DV Ti alloys including near α, α/β and β type can be synthesized by changing the percentage of each

constituent in y elements (Fe, Co, Ni, B, Si, etc.).

Despite the superior microstructures of the DV Ti alloys over the conventional as well as the supersaturated microcrystalline alloys, an optimization of mechanical properties in these alloys can't be easily achieved through the optimization of the composition. However, the β type DV alloys rich in the late transition metals (Fe, Co, Ni, Cu) can be potentially important systems in the future.

5. RAPIDLY SOLIDIFIED MICROCRYSTALLINE Ti ALLOY

5.1 MICROSTRUCTURE

Besides the fine scale of the microstructures due to rapid quenching in the RS Ti alloys, the additional microstructural variation comes from the type of precipitate, and the history of the heat treatment. In this program, all RS Ti alloys contain one or more additives aiming at stable precipitates at the high temperature, which differentiate the RS Ti alloys from the conventional Ti alloys. The morphology of the precipitate is an important factor for the strength as well as the other structure-sensitive properties.

a) As-Quenched State

The prevalent microstructures in the as-quenched alloy are a cellular structure, martensite structure and acicular alpha structure. The cellular structure size at the cooling rate of ~10^6K/sec is less than 0.5 μm diameter. This structure has been observed in the Zr containing alloy, α/β type alloys and near-α type alloys. Secondly, the martensite structure with a fine scale is widely found in near-α, α/β alloy in the cellular structure. In the α-Ti alloys, the acicular plate simply becomes finer with increasing the cooling rate. Under the current cooling rate, the acicular cell

width is within 0.2 μm. The acicular structures are parallel to each other within the prior Beta grain.

Also, when the additive amount exceeds the maximum solubility (as shown in Table 1), the precipitate starts appearing in the as-quenched alloy. Typically, in the rare earth containing alloy, the precipitate deposits along the network shaped sub-grain boundary. As the rare earth amount increases, the sub-grain size becomes smaller. This is indicative of a relationship between the sub-grain formation and the precipitation in the RE alloys.

b) Aged State

The major difference between the conventional and the RS Ti alloys may be found in the age hardening behavior of RS Ti alloys whereas the behavior is absent in the conventional alloy except for the alloy containing Si. The age hardening in the RS Ti alloys occurs between 550-700°C within a few hours. The age temperature increases with increasing the degree of the alloying by the alloying elements. By contrast, the temperature decreases with decreasing the atomic size of the additive elements primarily due to the fact that the diffusivity of an additive element is fast for the small atom (interstitial diffusion). In the aged state, the initial fine scale martensite structure disappears and a lathe martensite structure emerges similar to that observed in the conventional as-cooled alloys. The morphology of a precipitate is the characteristic of each additive element. For example, Si addition to the alloy results in equiaxed precipitates along the grain boundary or the sub-grain boundary while B addition results in rod-shaped precipitate in a random fashion. Meanwhile, the rare earth precipitates (group IIIA,

IVA metal-RE metals) with an almost perfect spherical shape are scattered uniformly in the matrix at the initial stage. However, the rare earth oxide having a cuboidal shape is also uniformly distributed in the matrix. The analyses of the precipitates containing the group IIIA, IVA metals and the RE metals have been conducted by TEM, SEM, STEM, EDXS and ELS. The results show that the precipitate is tentatively identified as a non-oxide in nature and rich in the group IIIA, IVA metals and the RE metals. For example, the selected area diffraction pattern from the precipitate in Ti-5Al-3La and the Ti-5Al-2.5Sn-3La annealed at 700°C,2h, was compared with those from pure La, La_2O_3, La_3Al and Al_4La. It turns out that the pattern best matches that of Al_4La while no oxygen was found in the precipitate by EELS. Hence, the precipitate is tentatively identified to be Al_4La (orthothombic). Also, in the rare earth rich Ti-5Al-6Ce alloy annealed at 950°C, 2h, a large particle of a several microns was found to be Ce rich Al composition. Nevertheless, there is a good possibility that the oxygen is associated with the precipitate since the oxygen has a strong affinity with the rare earth metals as well as the group IIIA, IVA metals.

c) <u>High Temperature Annealing (800-950° C)</u>

The Ti alloy samples were exposed at high temperature below the α or β transus to study microstructures. The primary interest is in the morphology as well as the coarsening of a precipitate, grain growth and other structures such as twin, recrystallization, etc. In general, the annealing was performed at 800-950°C for 1-2 hours in a vacuum sealed tube. As a result, a significant coarsening of the Si and B containing precipitates has been observed, in which the

silicide precipitate is found along the grain boundary, but the boride precipitate was found to be random. The rare earth precipitates are very stable at the high temperature, though to some extent a precipitate free zone appears after the annealing (900-950°C,2h). At this stage, the precipitate has a wide range of a size distribution, but the average size remains less than 500 Å.

5.2 MECHANICAL PROPERTIES

In the first year, preliminary mechanical properties such as microhardness and bend ductility as a function of heat treatment have been studied using splat foils and ribbon materials. A systematic study on the isothermal as well as isochronal heat treatments has been made in order to understand the aging behavior and the high temperature softening behavior.

1) As-Quenched State

A significant hardness increase has been found in the as-quenched Ti alloy with an additive. This increment from the non-additive alloy processed by rapid quenching derives mainly from the solid solution strengthening by the additive element. A large lattice misfit in the Ti matrix can be created both by metalloids and by rare earth metals. Secondly, the strength increment for the same amount of additive is twice as large in α-Ti alloys as it is in α/β type alloys. It is possible that the additive atom in the β phase segregates to the grain boundary. The weak age response in α/β Ti alloys may be associated with the high diffusivity of the additive in β phase. Table 2 shows microhardness increase in various RS Ti alloys in the as-quenched state. Enormous increase is noted in the RE containing alloy. However, the hardness begins to decline for the excessive addition of the RE additive beyond ~1 at % RE.

TABLE 2**

RS Ti Alloy wt %	As-Quenched State Microhardness**, Gpa	Increment per at %	Atomic Misfit $(R_A-R_{Ti})/R_{Ti}$
Ti-17.5Zr	3.2		
Ti-17.6Zr-1.1Si	3.5	~9	-0.1
Ti-17.8Zr-2.2Si	3.9		
Ti-17.7Zr-0.42B	3.6	~13	-0.33
Ti-18.0Zr-0.85B	4.1		
Ti-5Al-2.5Sn	3.5		
Ti-5Al-2.5Sn-2Y	4.2	~20*	0.21
Ti-5Al-2.5Sn-3Ce	4.3	~22*	0.23
Ti-5Al-2.5Sn-3La	5.1	~47*	0.27
Ti-5Al-2.5Sn-1B	5.7	~11	
Ti-6Al-4V	3.6		
Ti-6Al-4V-2.2Si	4.1	~4	-0.10
Ti-6Al-4V-1B	4.5	~6	-0.33
Ti-6Al-4V-1C	4.8	~9	-0.38
Ti-6Al-4V-3La	3.9	~8*	

R_A: The radius of an additive atom

*: The first at % only

**: Data on the splat foils of 20 μm thick has an error of ±2%

In the third column, the increment is proportional to the atomic misfit within the same type of an additive.

2) Aged State

The age hardening in the Ti alloy containing Si has been known for a long time. Similarly, in a RS Ti alloy which is highly supersaturated with an additive, a massive nucleation of a GP zone-like precipitate through the age treatment provides an optimum morphology for the dislocation barrier. Therefore, the resulting age hardening is much stronger than that in the conventional Ti alloy for

the same amount of the additive concentration. It turns out that age hardening exists in the Ti alloys containing either metalloids or rare earth metals or both. However, there are many differences between the two types of the precipitates by the metalloids and the rare earth elements.

a. Metalloid Containing Precipitate

RS Ti alloys containing a boride or a silicide precipitate show a maximum age hardening between 550-700°C within a few hours. The maximum age hardening temperature is directly related to the degree of alloying by the elements such as Zr, Mo, Al, etc. The strength of the aged alloy at the maximum value is as much as 20% higher than that of the as-quenched alloy and ~100% higher than that of the non-additive alloy.

As is the case in the conventional Ti alloy, RS Ti alloy undergoes overaging. This overaging characteristics are associated with the alloy elements. It has shown that Zr and Sn modified the overaging behavior by delaying or slowing down the coarsening process. Another very distinctive aging behavior in Ti alloys containing B is that two aging peaks appear in a sequence during the isothermal annealing. It seems that the first aging peak is attributable to a metastable precipitate.

b. Rare Earth Precipitate

The Ti alloys containing the rare earth metals exhibit a similar age hardening to that of the metalloid precipitates. Although two different types of the RE particles have been reported in RS Ti alloys, i.e., the rare earth oxide and the rare earth precipitate, no age hardening has been known to be

caused by the oxide particle. However, the new precipitates which contain the group IIIA, IVA metals and rare earth metals (but not oxygen) exhibit a strong aging behavior. The strength increase at the maximum age hardening ranges from 20 to 50% from that of the as-quenched state. Also, an addition of Zr to the alloy minimizes an overaging. The precipitate size at this stage is 50-100 Å which is in the range of a semi-coherency. The atomic size effects continue to show in the aged alloys containing the rare earth elements. For example, a linear relationship between the atomic size misfit and the microhardness was observed in the Ti-5Al-2.5Sn-3La (-2Y,3Ce) alloys. No double aging behavior was observed in the rare earth containing alloys.

3) <u>High Temperature Annealing</u>

Isochronal annealing (2h) for various RS Ti alloys show an abrupt softening in hardness near 800°C, which consequently appears to be related to the coarsening of a precipitate. The hardness nearly returns to the level of the as-quenched state after the 900-950°C, 2h annealing, but is much higher than that of the non-additive alloy. The details of the coarsening behavior will be discussed in the next section.

4) <u>Bend Ductility</u>

The geometry of the ribbon or the splat foil allows only the bend ductility test, though the elongation and the fracture toughness are the desirable properties to be studied. The bend ductility of α-Ti alloys was determined as a function of heat treatment by both yield strain for the ductile state and fracture strain for the

brittle state. The minimum bend ductility coincides with the maximum age hardening, and vice versa. However, at 800°C, the ductility returns to that of the as-quenched state while the strength remains as much as 20% higher than that of the as-quenched state. Therefore it is anticipated that the bulk alloy gains a significant strength from the precipitate hardening after the high temperature consolidation while maintaining a high level of a ductility in this type of RS Ti alloys.

5) Effects of Cooling Rate

It is well known that the relationship between the cooling rate and the individual microstructural refinement has been expressed by an exponential equation. On the contrary, a well-defined relation does not exist between the cooling rate and the mechanical properties. In fact, a mechanical property is related to the cooling rate in a complicated manner through the microstructures such as a supersaturation of an additive, martensite structure, precipitate, grain size, cellular structure, dendritic structure, etc. It has been observed that the strength depends on the thickness of the sample which in turn is a linear function of the cooling rate. For example, in Ti-5Al-2.5Sn-3Ce (-3La,1B) isochronal annealing for 500-900°C, 2h, was conducted on two different samples of 20 μm and 40 μm thick respectively. The results show that in the as-quenched as well as aged state the microhardness of 20 μm sample is ~10% higher than that of 40 μm sample. Theoretically, the cooling rate difference between the two samples is a factor of two.

On the other hand, in the ribbon sample of 40 μm thick, the hardness is systematically lower than that of the splat foil of 40 μm

thick. As a matter of fact, the cooling rate of the ribbon is roughly a half of that of the splat foil for the same thickness, which means that the ribbon of 40 μm thick is equivalent to the splat foil of 80 μm thick in terms of the cooling rate. Currently, the mechanical properties are being studied with ribbon materials.

5.3 SECOND PHASE PARTICLE COARSENING

The success of the alloy design for RS Ti alloys primarily lies with the stability of the second phase at high temperature. The second phase available in RS Ti alloys varies from the metalloid and the rare earth compounds. A study on the coarsening of the second phase in Ti-5Al-2Si has been conducted at a temperature range from 600 to 800°C for a maximum 100 h. The precipitate known to be Ti_5Si_3 ($D8_8$ structure) takes a nearly spherical shape in the RS Ti alloy in contrast with a rod shape in a single crystal Ti alloy.

The experimental results shows that at the temperatures of 700-800°C, the coarsening data fits the Wagner's lattice diffusion model, which means that the cube of the mean particle diameter is linearly proportional to the time. Therefore, the bulk diffusion is the dominant mechanism in the Ti-5Al-2Si at this temperature range. The second column of Table 3 shows the product of the effective diffusion coefficient (D_e) and the interfacial free energy (γ) between the particle and the matrix which was obtained from the $\bar{d}^3$ vs st, where $\bar{d}$ and t are the mean diameter of the particle and the soaking time.

TABLE 3

Temperature (°C)	$D_e \cdot \gamma$ (J/sec)	D_e (effective diffusion coefficient) (cm^2/sec)	Self-diffusion coefficient of α-Ti cm^2/sec
600	(1.3×10^{-16})	($\sim 10^{-12}$)	-----

700	2.6×10^{-15}	$\sim 10^{-11}$	9.8×10^{-14}
800	4.2×10^{-14}	$\sim 10^{-10}$	1.6×10^{-12}

Instead of inserting the diffusion coefficient value of Si into the Wagner's equation to obtain γ value, the γ was assumed in order to estimate the order of magnitude of the effective diffusion coefficient. If the interfacial free energy for the incoherent Ti_5Si_3 is assumed to fall between 0.5-1.5JM^{-2}, the D_e values listed in the third column are obtained. Also, the self-diffusion values in the last column were calculated from an activation energy, 58K cal/mole and a pre-exponential term, 1.0 cm^2/sec. From the comparison between the two values, the D_e value is two orders of magnitude larger than that of the self-diffusion value. Furthermore, considering the fact that the D_e is a coupled diffusion coefficient, the actual diffusion coefficient of Si in Ti might be higher than the D_e value listed in this table. In fact, the results for 600°C better suit an arbitrary power relation, $d^{3.5}=k.t.$ The exponent 3.5 is an average of the lattice diffusion mode, 3, and the high angle grain boundary diffusion mode, 4. Again, from the microstructural observation, a high density of martensitic structure and subgrain structure was identified, in which the subgrain size ranges from 0.1 μm to 0.5 μm diameter. As a result, it is likely that at this temperature, the low angle boundary diffisuion may be a dominant mechanism.

On the other hand, the TEM and SEM micrograph of the rare earth containing alloys soaked at 900-980°C indicate that the second phase particle is extremely stable. Presently, the study of the second phase particle coarsening in a Ti-Al-Y(-La,-Ce) alloy is underway. Also, it is interesting to see any correlation between the coarsening and the atomic size of the additive element since there is an indication that the atomic size of the additive elements is related to the strength at the entire annealing temperature range. It is presumed that the diffusivity of the larger rare earth atom in Ti is lower than

that of the smaller atom.

6. MELT SPINNING PROCESSES FOR Ti ALLOYS

There have been many different melt spinning processes for Ti alloys. They are the pendant drop melt extraction, the crucible melt extraction processes and, recently, the arc plasma melt spinning process. The former two processes are slightly different from the normal melt spinning process in that the molten pool undergoes dragging by the spinning disk surface. Therefore, the product of these techniques is a half circled wire. As a result, the cooling rate is not as high as that achieved by the ordinary melt spinning. On the other hand, the arc plasma melt spinning technique can produce a thin ribbon and, as a result, achieve a high cooling rate of $\geq 10^6$ k/sec. Currently, a pilot scale melt spinner of this kind is being built under this program. As shown in Figure 1, the spinner consists of three functional parts. They are melting compartment, spinning compartment, and ribbon processing compartment. The detailed features are described below.

a. Melting Compartment

Pre-melted ingot alloy as starting materials is charged directly into a cold copper crucible and additional granule alloy is continually supplied by an auto-feeder to maintain the molten alloy level. The melting is achieved by arc plasma using a non-consumable tungsten electrode under argon or helium atmosphere. The electrode swings round above the melt at a maximum of 150 turns/min. to ensure the homogeneity of the melt temperature. The power is supplied by a welder powder supply (32KW,50-750A). When the melt is super-heated, additional gas is introduced into this compartment to inject the molten alloy through an orifice centered at the bottom of the crucible.

b. Spinning Compartment

This compartment comprises two spinning disks, i.e., one has a flat surface and the other has a series of serrated grooves on the surface, and a disk brush. The spun ribbon is thrown into the ribbon processing chamber through an opening between the spinning compartment and the ribbon processing chamber. The disk provides a variable speed at the maximum surface speed of ~45m/sec.

c. Ribbon Processing Compartment

The produced materials have two forms: flakes or regular spun ribbons. These materials can be packed in a can under inert gas atmosphere by a pair of gloves attached to the chamber door. Brittle ribbons can be pulverized by a small hammer-mill inside the chamber beforebeing packed in a vacuum-tight container. However, when the ribbons are too ductile to break into particulates, they can be treated through hydrogen embrittlement or cut into pieces by a mechanical chopper. An example is shown in this report.

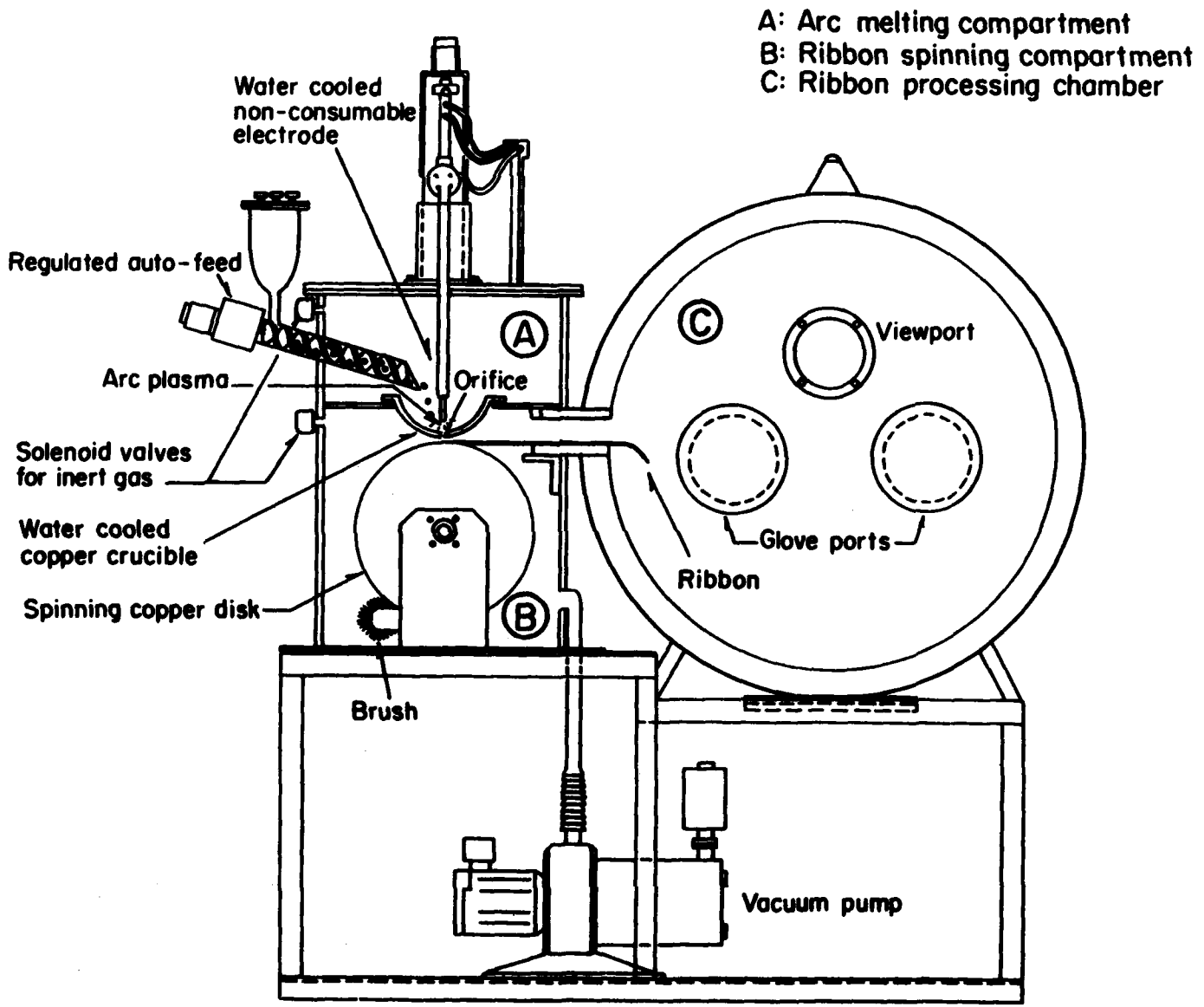

Fig. 1. Schematic drawing of pilot arc plasma melt spinning unit.

TECHNICAL ARTICLES

1. C.S. Chi, S.H. Whang, "Effects of Novel Additives (B, Ce) on Microstructural & Mechanical Properties in Rapidly Solidified Alpha Ti Alloys," TMS-AIME paper selection, October 1983, Paper No. F83-14

2. S.H. Whang, Y.Z. Lu, "Aging Behavior of Devitrified Ti Rich Alloys Containing Metalloids," Proceedings Third Conf. on Rapid Solidification Processing, R. Mehrabian, ed. (1983) 286-290

3. S.H. Whang, "Glass Forming Ability for Binary Alloy Systems by Modified T-C Map in Relation to Phase Diagram," Proc. Intl Conf on Liquid and Amorphous Metals. Aug 1983, UCLA, Los Angeles CA. In press.

4. S.H. Whang, "Glass Forming Property of Ti-Zr-Si System Determined by Temperature-Composition Map," submitted to Scripta Met.

5. B.C. Giessen, S.H. Whang, "Metallic Glass Formation Diagram," Proc. Mat. Res. Soc. Symp. Vol 19 (1983) 289-294

6. Y.Q. Gao, S.H. Whang, "Crystallization Behavior of Binary Metallic Glasses Containing Pt," Submitted to J. Non-Cryst. Sol.

7. S.H. Whang, B.C. Giessen, "Mechanical Chopper for Rapidly Quenched Metallic Ribbon," Materials Letters, in press.

TMS paper selection

PAPER NO.

F83-14

EFFECTS OF NOVEL ADDITIVES (B, Ce) ON MICROSTRUCTURAL AND MECHANICAL PROPERTIES IN RAPIDLY SOLIDIFIED ALPHA Ti ALLOYS

by

C. S. CHI

S. H. WHANG

THE METALLURGICAL SOCIETY OF AIME

420 Commonwealth Drive, Warrendale, PA 15086 • 412/776-9000

EFFECTS OF NOVEL ADDITIVES (B,Ce) ON MICROSTRUCTURAL AND MECHANICAL PROPERTIES IN RAPIDLY SOLIDIFIED ALPHA Ti ALLOYS

C.S. Chi and S.H. Whang

341 Mugar, Institute of Chemical Analysis
Northeastern University
Boston, Massachusetts 02115
USA

Small amounts of novel additives (B,Ce) were incorporated in α-Ti based alloys via rapid liquid quenching. Subsequent heat treatment at a temperature range of 500-700° C resulted in a strong aging response in conjunction with uniform and fine dispersoids (∿100 Å) in the matrix. EDXS spectrum of a large precipitate in Ti-Al-Ce shows that the precipitate is rich in Al and Ce, which indicates a strong possibility of a Al-Ce compound formation. Microstructure of the alloy containing Ce continues to show that most precipitates are under ∿0.1 μm after high temperature annealing (900° C,2h). The aged strength in the alloys containing 1 at.% Ce and 4 at.% B is 6.0 and 7.0 GPA (DPH) respectively. Both Ce and B containing alloys annealed at 900° C, 2h demonstrate moderate strength in agreement with the microstructure observed.

Introduction

Through rapid solidification processing (RSP) microstructure and strength of RS alloys have improved in a great deal as demonstrated in Fe,Al based alloys and superalloy.(1,2) Nevertheless, little study has been made in Ti alloy systems primarily because of their strong chemical reaction with crucible materials, which has been a stumbling block for the production of RS Ti alloys at will. However, preliminary study indicates that the similar microstructural refinement (3-6), novel morphology of precipitate (4) and unique mechanical properties can be achieved in RS Ti alloys. Drastic increase in strength was noted in RS Ti alloy containing B and Si at the aged state. A recent study in this area includes synthesis of RS Ti alloys containing metalloids or pure Ti with rare earth metals (Y,Er) as additives. (7) However, the role of rare earth metals in pure Ti is to form segregated particles or to give off rare earth oxide particles through the reaction with free oxygen. So far, no systematic investigation of precipitation hardening by rare earth compounds in relation to high temperature properties has been reported. In this paper, we report on two different types of α-Ti alloys containing metalloid (B) or rare earth metals (Ce). Both additives do not have solubility in Ti at low temperature, but they are quite different in atomic size and chemical interaction with Ti. Ce forms a monotectic system with Ti (Figure 1) with a very stable miscibility gap in the liquid whereas B yields very stable intermetallic compounds between Ti. In the following, age hardening behavior and microstructural characteristics of these alloys are presented.

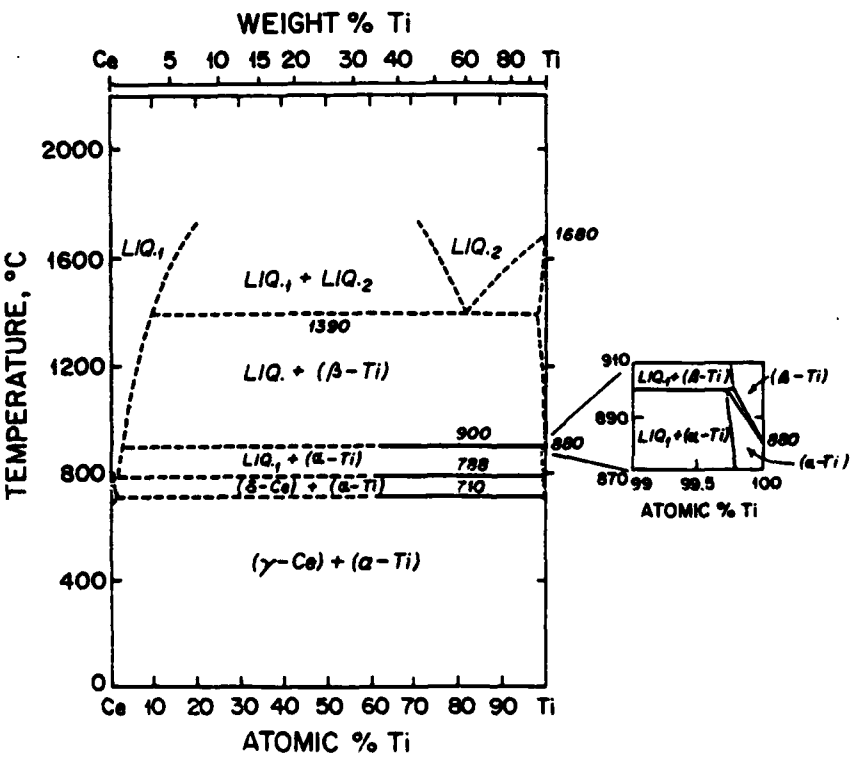

Figure 1 - Ti-Ce phase diagram

Experiments

The reactive nature of Ti alloys means that they require special care during melting, solidification and heat treatment. In particular, serious contamination by crucible materials, electrode, or excessive interstitials (O,N), etc., are subjects of concern. Hence, melting, splating, and spinning are performed in a cold copper hearth under positive inert gas atmosphere. All Ti alloys were prepared from pure elements having grades of 99.9 for Ti and 99.99 for other elements. Subsequently, for heat treatment, samples were wrapped with tantalum foil and sealed in a quartz tube under vacuum. Microstructural study was carried out by TEM, SEM or electron microprobe. TEM sample preparation was made by either electropolishing using acid solutions or ion bombardment technique. Microhardness was measured by Vicker's diamond pyramid hardness tester using 50g load and 30 sec duration. The hardness value was determined by averaging more than ten indentations from one specimen. The standard deviation of the data was ~±2%. Bend ductility was obtained by measuring the diameter of the half circle of the sample foil at failure. The strain to failure was calculated using an approximate relation (8).

Results

Alloy Systems

Typical α-Ti alloys were selected as base alloys; Ti-Al, Ti-Al-Sn and Ti-Al-Zr-Sn. The amount of Ce and B in the alloys ranges from 0.5 to 6 wt. %. However, the maximum extended solid solubility of Ce and B for the cooling rate of ~10°K/sec is ~0.6 at % and ~3 at % each. Excess addition of these elements results in precipitate (~50 Å) at the sub-grain boundaries in as-quenched state.

Microstructures

TEM micrographs of quenched Ti alloys from liquid exhibit common features existing in other RS alloys such as microstructural refinement, supersaturated phase, and extremely fine precipitate or cluster if present. Although all Ti alloys studied share these fundamental aspects, the details of the microstructure are different depending on the type of additive element used.

Ti-Al-(Sn)-Ce. It is important to understand any chemical reaction that might occur during heat treatment due to the additive elements in α-Ti alloys. Splat foil of Ti-5Al-6Ce was prepared and annealed at 950° C for 24h under vacuum. The annealed specimen shows under SEM that some precipitates are as large as several microns diameter as shown in Figure 2(a). Subsequently, the precipitate was checked with energy dispersive x-ray spectroscopy to identify the constituents. The results are shown in Figure 2(b) and (c), in which the spectrum from the precipitate reveals proportionally strong Al and Ce peaks whereas weak Al and almost negligible Ce peaks are present in the spectrum from the matrix. This is an indication that the precipitate might take the form of a compound existing in the binary Al-Ce phase diagram

As a practical alloy, Ti-5Al-2.5Sn-3Ce was investigated by TEM with respect to the microstructures for the different stages of heat treatment. The as-quenched micrograph (3(a) and (b)) exhibits very sharp alpha grain which is divided by network shaped sub-grains. Also noticed was extremely fine precipitate at the sub-grain boundaries (~50- ~100 Å). At the aged state, a high density of fine particles (~100 Å) are uniformly distributed in the grain (4(a) and (b)) preceded by the disappearance of the sub-grain boundary. No segregation to the grain boundary was observed. In order to

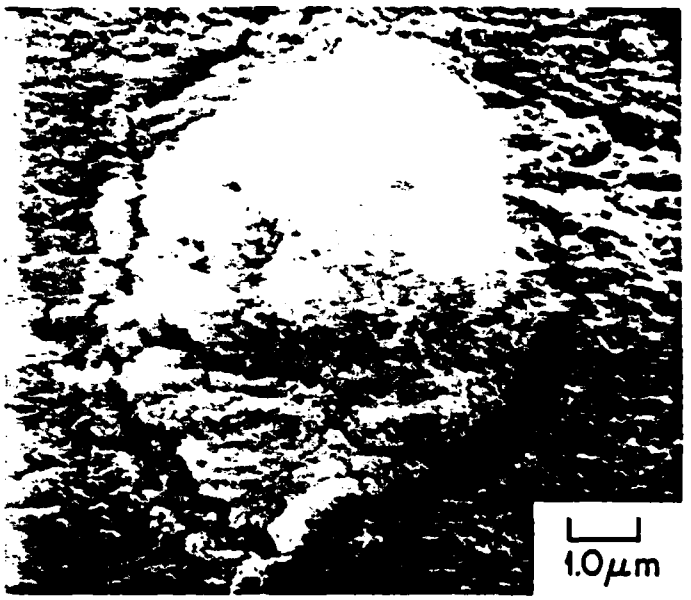

Figure 2(a) - SEM micrograph of a precipitate in annealed Ti-5Al-6Ce (950°C,24h)

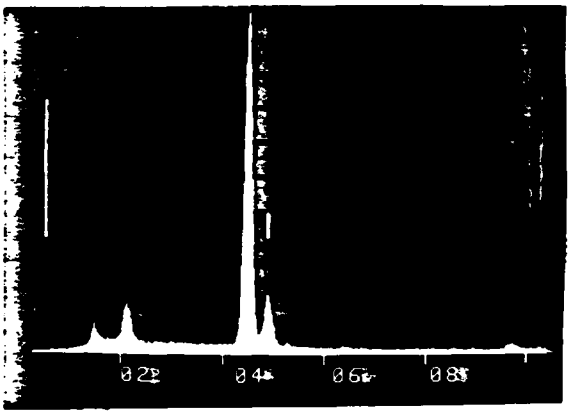

Figure 2(b) - EDXS of the matrix of the same alloy

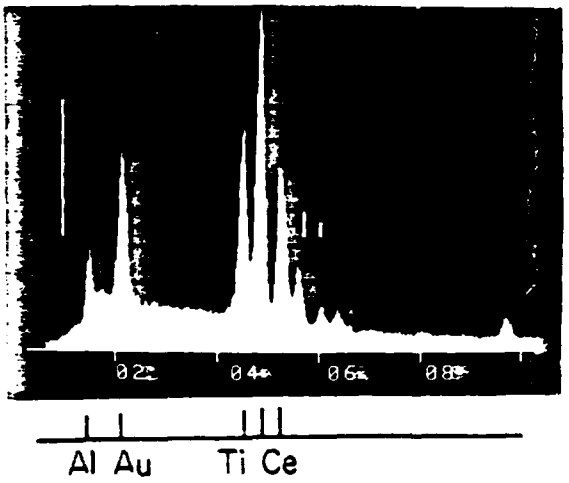

Figure 2(c) - Energy dispersive x-ray spectrum of the precipitate. High concentration of Al and Ce

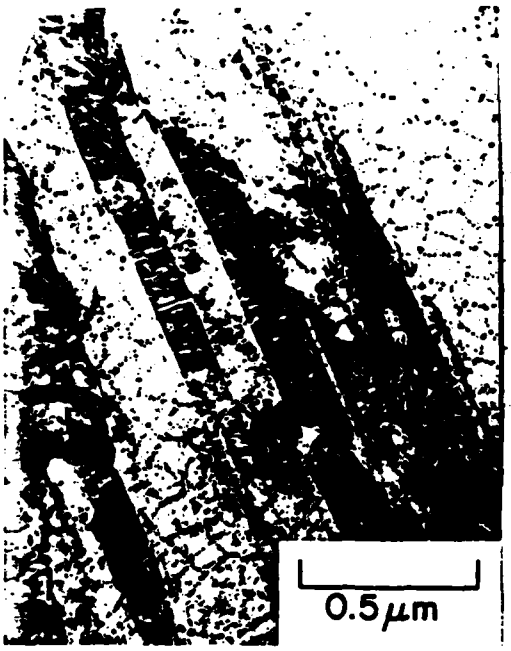

Figure 3(a) - TEM micrograph (BF) of AQ Ti-5 Al-2.5Sn-3Ce

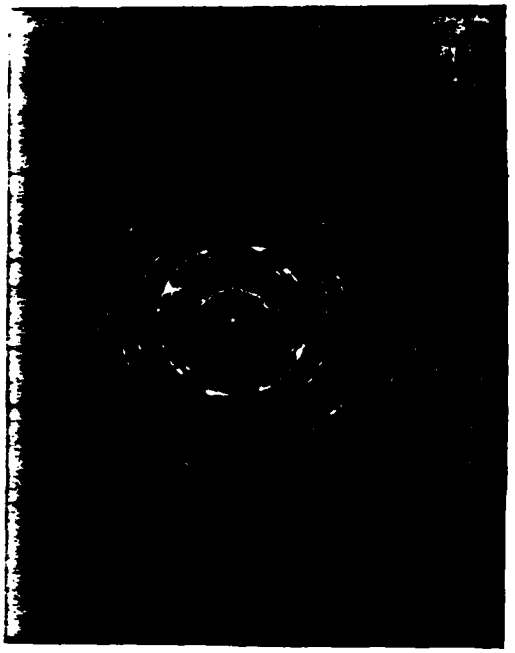

Figure 3(b) - Diffraction pattern from Figure 3(a)

Figure 4(a) - Bright field micrograph of aged Ti-5-2.5-3Ce (700°C, 2h)

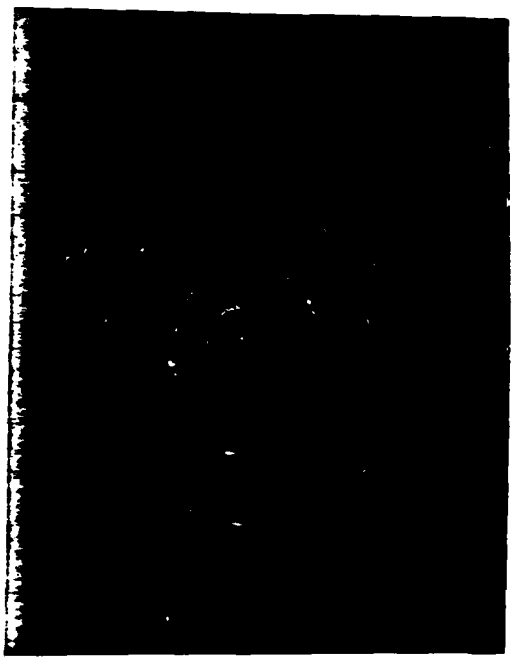

Figure 4(b) - Diffraction pattern from Figure 4(a)

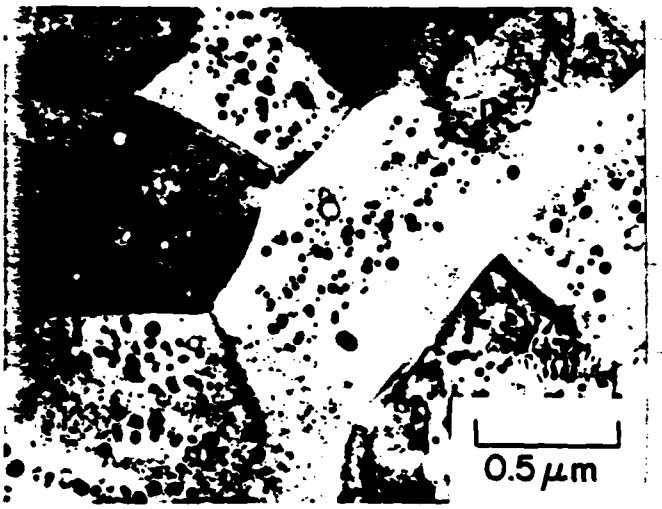

Figure 5 - BF micrograph of annealed Ti-5-2.5-3Ce (900°C, 2h)

find the coarsening behavior of the particles, the specimen was annealed at 900°C, 2h, which is shown in Figure 5. Still, most particles remain under ~0.1 μm diameter but a precipitation free zone starts to appear along the grain boundary.

Ti-Al-Sn-B. Previously, the boron containing Ti alloy was found to be different in microstructure and age hardening behavior from the Si containing alloy (9). As-quenched Ti-5Al-2.5Sn-1B alloy (Figure 6(a) and (b)) produces much finer acicular structure than that in the Ce containing alloy and thereby results in a semi-continuous diffraction ring. A trace of boride formation in the as-quenched state was confirmed from the bright spots inside the first ring.

High temperature annealing (900° C, 2h) induces grain growth as well as coarsening of needle-like boride precipitate (Figure 7(a) and (b)). The boride and grain size at this stage are 0.05-0.5 μm long and 0.2-0.5 μm diameter respectively. The orientation of boride precipitate appears random because many of them lie across the grain boundary or have different orientations in the same grain. The needle shape boride is only found in RS Ti alloys so far.

Mechanical Properties

In the previous section, the morphology of precipitate resulting from heat treatment at the intermediate temperature forecasts a significant change in mechanical properties. In this paper, precipitation hardening phenomenon in RS Ti alloys containing Group IIIA and IVA metals (Al,Sn,Ge) will be presented.

As-Quenched State. Supersaturated solid solution of α-Ti alloys containing a small quantity of additive element via RSP gives rise to a significant increase in strength primarily due to solid solution strengthening, and to a lesser extent due to microstructural refinement (Figure 8). For example, despite microstructural refinement, no significant increase in strength for RS Ti-5Al-2.5Sn was observed. The increase is 30% for the Ce containing alloy and 70% for the B containing alloy from AQ Ti-5Al-2.5Sn alloy. The difference between the two alloys is largely due to high concentration of B (.4 at %) rather than that of Ce (.1 at %). Also, it is noticed that Zr addition further increases strength due to alloying effect.

Figure 3(a) - TEM micrograph (BF) of AQ Ti-5 Al-2.5Sn-3Ce

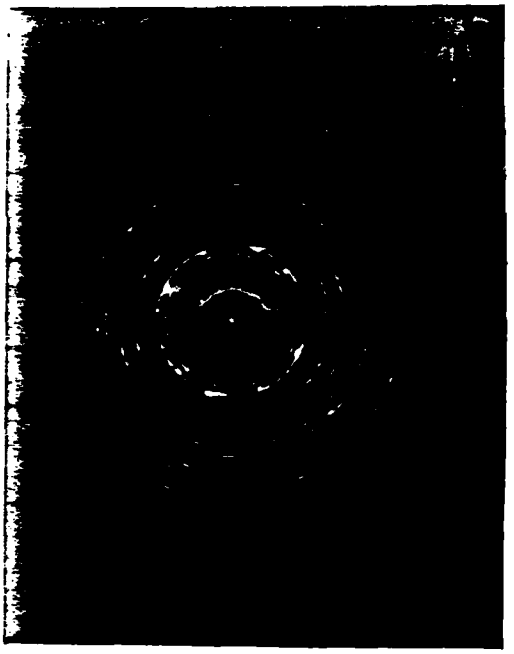

Figure 3(b) - Diffraction pattern from Figure 3(a)

Figure 4(a) - Bright field micrograph of aged Ti-5-2.5-3Ce (700°C, 2h)

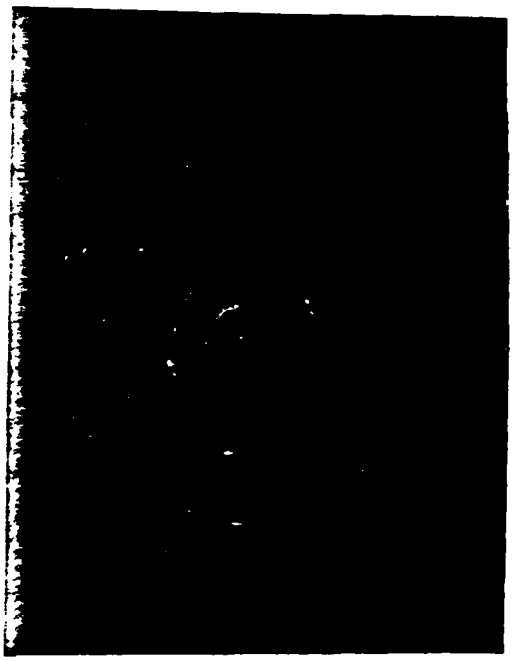

Figure 4(b) - Diffraction pattern from Figure 4(a)

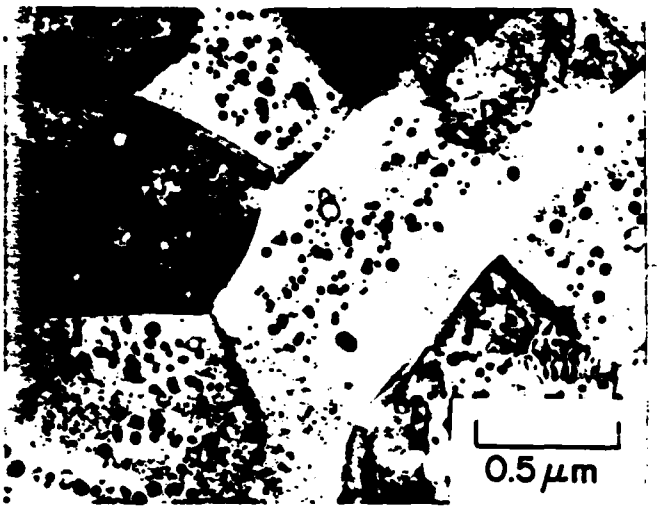

Figure 5 - BF micrograph of annealed Ti-5-2.5-3Ce (900°C, 2h)

find the coarsening behavior of the particles, the specimen was annealed at 900°C, 2h, which is shown in Figure 5. Still, most particles remain under ~0.1 μm diameter but a precipitation free zone starts to appear along the grain boundary.

Ti-Al-Sn-B. Previously, the boron containing Ti alloy was found to be different in microstructure and age hardening behavior from the Si containing alloy (9). As-quenched Ti-5Al-2.5Sn-1B alloy (Figure 6(a) and (b)) produces much finer acicular structure than that in the Ce containing alloy and thereby results in a semi-continuous diffraction ring. A trace of boride formation in the as-quenched state was confirmed from the bright spots inside the first ring.

High temperature annealing (900° C, 2h) induces grain growth as well as coarsening of needle-like boride precipitate (Figure 7(a) and (b)). The boride and grain size at this stage are 0.05-0.5 μm long and 0.2-0.5 μm diameter respectively. The orientation of boride precipitate appears random because many of them lie across the grain boundary or have different orientations in the same grain. The needle shape boride is only found in RS Ti alloys so far.

Mechanical Properties

In the previous section, the morphology of precipitate resulting from heat treatment at the intermediate temperature forecasts a significant change in mechanical properties. In this paper, precipitation hardening phenomenon in RS Ti alloys containing Group IIIA and IVA metals (Al,Sn,Ge) will be presented.

As-Quenched State. Supersaturated solid solution of α-Ti alloys containing a small quantity of additive element via RSP gives rise to a significant increase in strength primarily due to solid solution strengthening, and to a lesser extent due to microstructural refinement (Figure 8). For example, despite microstructural refinement, no significant increase in strength for RS Ti-5Al-2.5Sn was observed. The increase is 30% for the Ce containing alloy and 70% for the B containing alloy from AQ Ti-5Al-2.5Sn alloy. The difference between the two alloys is largely due to high concentration of B (~4 at %) rather than that of Ce (~1 at %). Also, it is noticed that Zr addition further increases strength due to alloying effect.

Figure 6(a) - TEM micrograph of AQ Ti-5Al-2.5Sn-1B

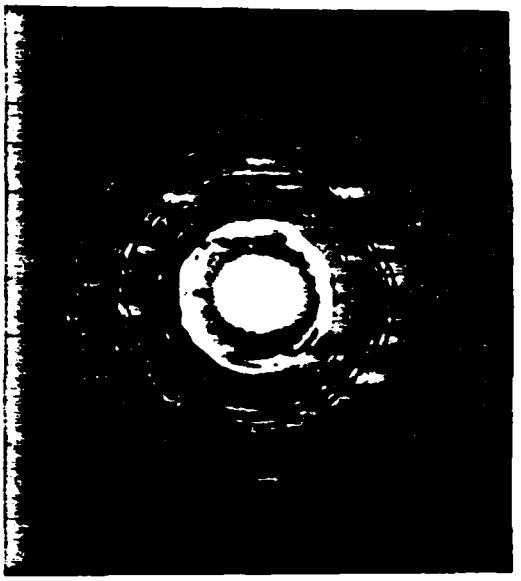

Figure 6(b) - Diffraction pattern from Figure 6(a)

Figure 7(a) - BF micrograph of annealed Ti-5-2.5-1B (900°C, 2h)

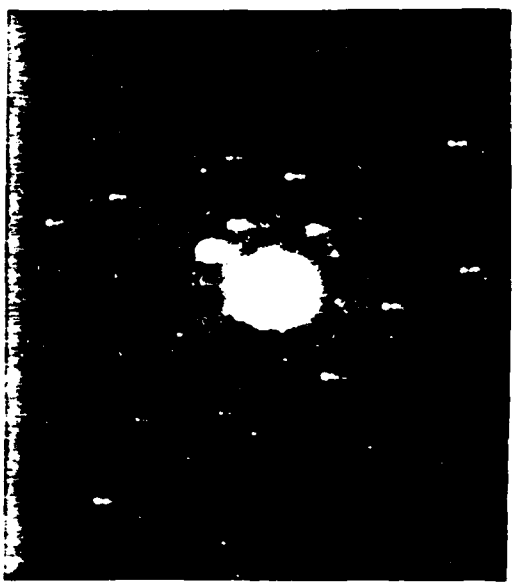

Figure 7(b) - Diffraction pattern from Figure 7(a)

Age Hardening. In Figure 8, the alloys were aged at 600° C as a function of time. Both Ce and B containing alloys show a strong age response at this temperature, which is consistent with microstructural observation in Figure 4(a). The hardness increase in the aged alloy is as much as 20-40% from the as-quenched state. Therefore, the maximum strength at the age state is as much as twice that of as-quenched Ti-5Al-2.5Sn. After 20h annealing at this temperature, a significant softening occurs due to overaging. Beyond the strength increase due to the precipitation, it is important to understand the origins of the precipitates in the two α-Ti alloys. The precipitate in the B containing alloy having a large lattice parameter is basically titanium boride while that in the Ce containing alloy is in the form of a compound rich in Al and Ce.

Isochronal Annealing. In order to conduct isochronal annealing, each specimen was annealed for two hours at temperatures from 500° C to 900° C. At the same time, this annealing experiment was performed on two kinds of samples, i.e., 20 μm thick and 40 μm thick. The results are shown in Figure 9 and 10. By and large, maximum strength occurs at 700° C and softening starts at 800° C. For the entire temperature range, the thinner sample maintains higher strength by 10% than the thicker one does. The thickness of the sample is inversely proportional to the cooling rate (10) which, in turn, is related to the degree of supersaturation of additives and microstructional refinement. The thickness effect is relatively large in as-quenched as well as aged state.

Bend Ductility. Ductility is one of the critical parameters in the process of the evaluation for the suitability of a practical alloy. Owing to the geometry of as-quenched sample and the premature failure of ribbon materials, a bend ductility test was performed. Ductility and strength are two opposing parameters in which the relation is not a simple form of function. In Figure 11, as age hardening proceeds, bend ductility rapidly decreases and reaches a minimum value at 700° C where age hardening attains a maximum value.

Discussions

Ti alloys containing RE metals have different aspects from those containing metalloids in terms of alloy chemistry. The rare earth elements have very limited solubility in Ti due to their large atomic size whereas the metalloid has small atomic size. In both cases, the size difference from Ti atom is more than 15%. Secondly, chemical interaction between RE elements and Ti is insignificant while that between the metalloid and Ti is strong due to the large electronegativity difference. These differences are well reflected in the phase diagram viz. very stable intermetallic compounds exist in the Ti-B diagram whereas in that for Ti-Ce, a very stable liquid miscibility gap and no compound phase are found. On the other hand, maximum extended solid solubility of Ce in Ti is less than three times that of the maximum equilibrium value, which is considered to be the low limit of the extended solid solubility in RSP. The reason for this may be as follows: as a monotectic system, Ti-Ce phase diagram has in particular a large liquid-solid mix zone between horizontal liquidus and solidus lines. That makes it difficult for an additive atom to remain unsegregated during rapid cooling. The comparison between the role of B and Ce in RS α-Ti alloys is summarized in Table 1.

Precipitate hardening was also found in other α and near-α-Ti alloys containing Y,La or Nd (11). Age hardening also was obtained when Al was replaced by Sn or Ge since these elements interact with RE metals in a similar manner. Although fine precipitate can be obtained by RSP, the unique effects may be found in the shape change of a precipitate. For

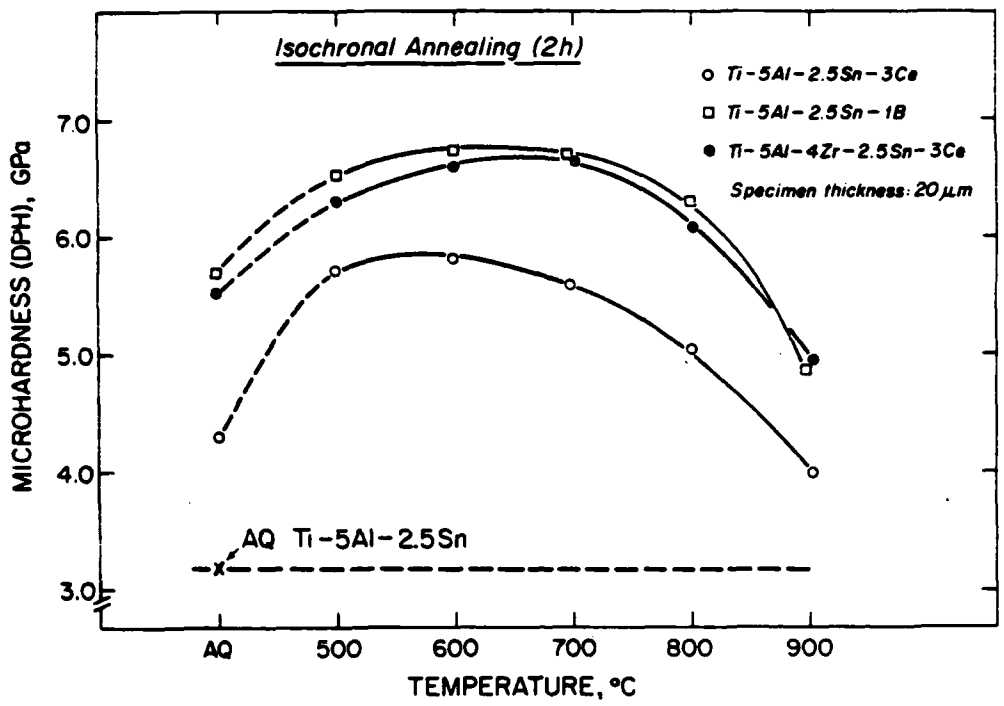

Figure 10 - Isochronal annealing (2h) of Ti-5-2.5-1B(-3Ce) and Ti-5-4-2.5-3Ce. Specimen thickness: 20 μm

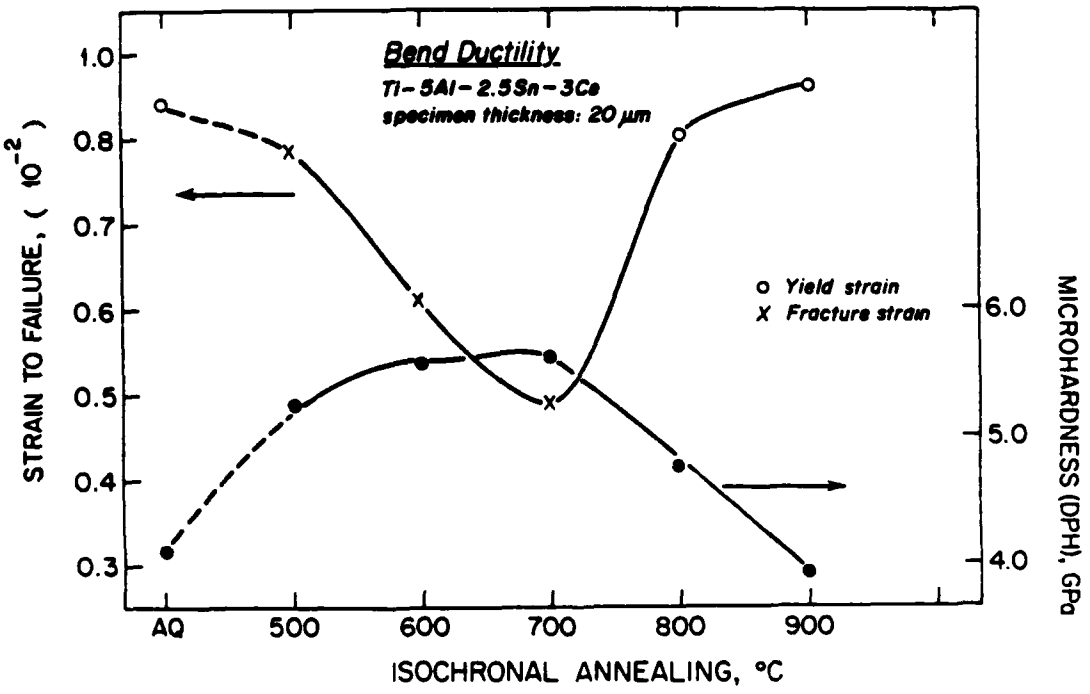

Figure 11 - Bend ductility vs isochronal annealing temperature in Ti-5-2.5-3Ce

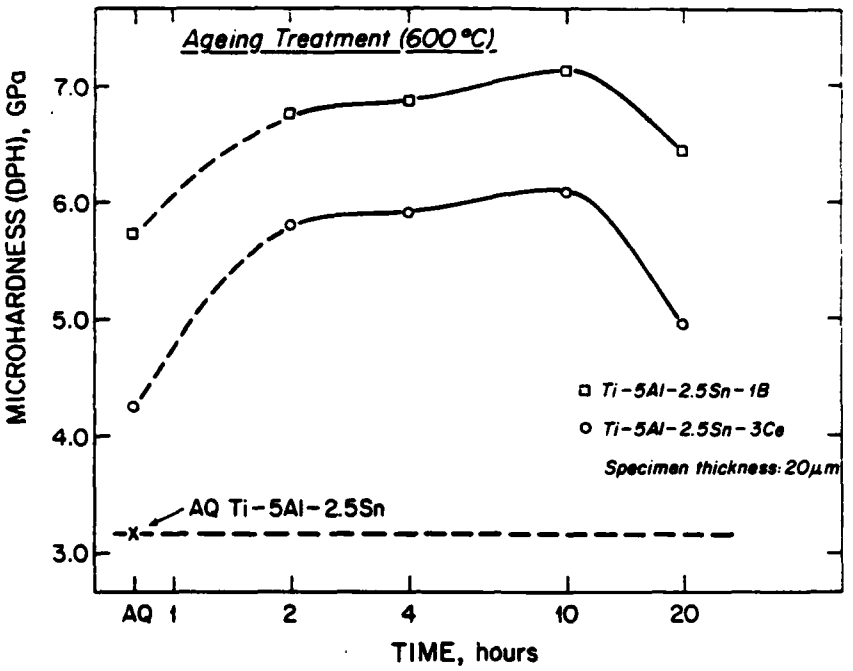

Figure 8 - Age hardening of Ti-5-2.5-1B(-3Ce) at 600° C. Specimen thickness: 20 μm

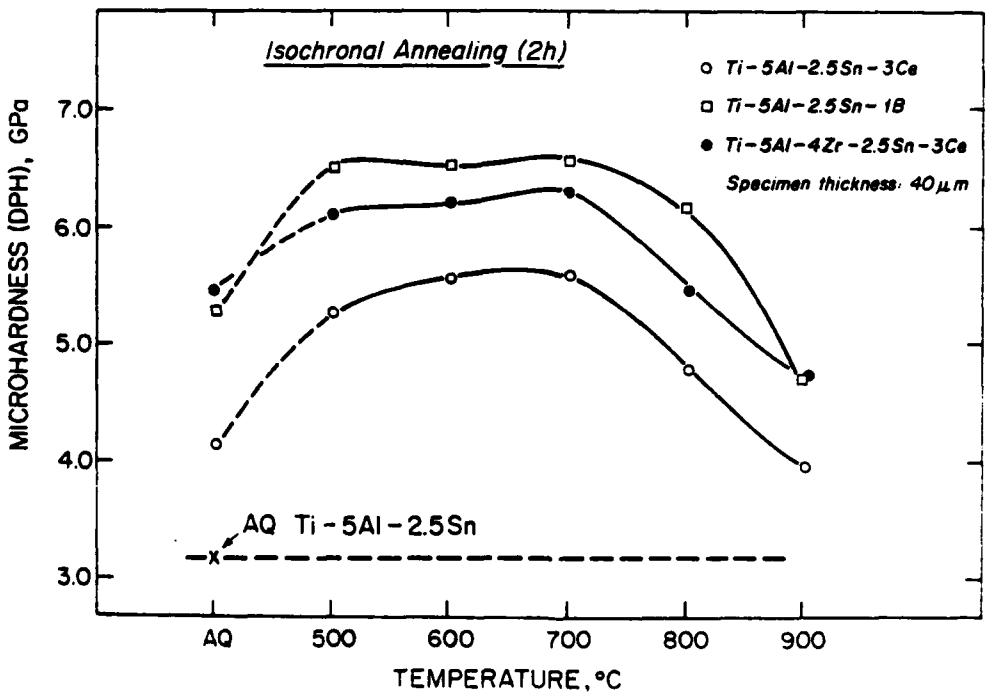

Figure 9 - Isochronal annealing (2h) of Ti-5-2.5-1B(-3Ce) and Ti-5-4-2.5-3Ce. Specimen thickness: 40 μm

TABLE 1

Additive	Probable Site in AQ Ti	Compound Phase Type	Age Hardening	Precipitate Shape	Morphology
B	Octahedral	Ti-B	Yes	Needle shaped	Random
Ce	Substitutional Site	Ce-Al,Sn,Ge	Yes	Spherical	Fine & uniform

example, in a Ti alloy containing Si, only needle shaped or high aspect ratio of silicide is found in conventional alloys whereas equiaxed or spherical shaped precipitate repeatedly is observed in RS Ti alloys. The reason for the modification of the shape may be that the coherent particle becomes easily incoherent due to the high density defects available in the as-quenched alloy. On the contrary, in the B containing alloys, it is possible that the precipitate readily maintains semi-coherency in one direction (at least) and thereby reduce a significant amount of interfacial energy.

A good correlation between atomic radius ratio (ε_i) and hardness value for the aged sample was found, i.e., strength increase is linealy proportional to the atomic size ratio for the range from 1.2 to 1.3 ε_i. It is possible that strength increase may be very small near 1.15 ε_i if an asymptotic approach of the correlation line to the origin is assumed, which is in principle in agreement with Hume-Rothery's rule of solid solution. From the correlation in Figure 12, an empirical relation may be derived,

$$H = K\varepsilon_i C \text{ and } \dot{H}(\varepsilon_i) = KC \qquad 1(a)$$

Where H is hardness increase, C is concentration of a solute, K is constant, and $\varepsilon_i = (R_A - R_B)/R_{Ti}$; R_A, R_B are atomic radii of rare earth metals, A and B. Eq. 1(a) may be rewritten as

$$\sigma(\simeq \frac{H}{3.6}) = \beta\mu.\varepsilon_i^n C \qquad 1(b)$$

Where σ is yield stress increase, μ is shear modulus and n is unity. If μ is taken to be ~60 GPa, β of eq. 1(b) becomes ~12. This expression is analogous to Nabarro's (12) and Cottrell's (13) relations in which size effect is a major factor.

$$\text{i.e. } \sigma = \alpha\mu\, \varepsilon^n\, C \qquad (2)$$

Where α is a constant varying from 0.25 to 2.5 and n is $1 \leq n \leq 2$. Therefore, by assuming that $\varepsilon = \varepsilon_i$ and n = 1, β becomes five times larger than the largest α. Nevertheless, these two equations describe different correlation curves since in equation 1(b) ε_i is the only independent variable while in equation 2, C is the only variable. On the other hand, in Figure 12, it is unlikely that the correlation line remains linear for the entire ε_i range since a straight line cannot meet the origin, i.e., here, hardness value for AQ Ti-5Al-2.5Sn. Hence, in equation 1(b) n is approximately unity for a limited range.

Finally, strength increase in as-quenched alloy is presumably attributed to two factors. One is microstructure refinement and the other is the increased solubility of a solute beyond the equilibrium value due to the rapid solidification. Particularly, since both the extension of the solubility and the refinement of microstructure are proportional to the cooling rate, the cooling rate increase in an alloy containing insoluble additives is expected to show rapid enhancement in strength due to the combined effects from the extended solubility and the microstructure refinement.

For instance, in Al alloys (15) microstructure refinement alone by doubling the cooling rate increases hardness by ~4% while in Ti-Al-Sn-RE the increase is as much as ~10% due to the solubility increase alone, which is estimated from the relationship between the sample thickness and hardness value.

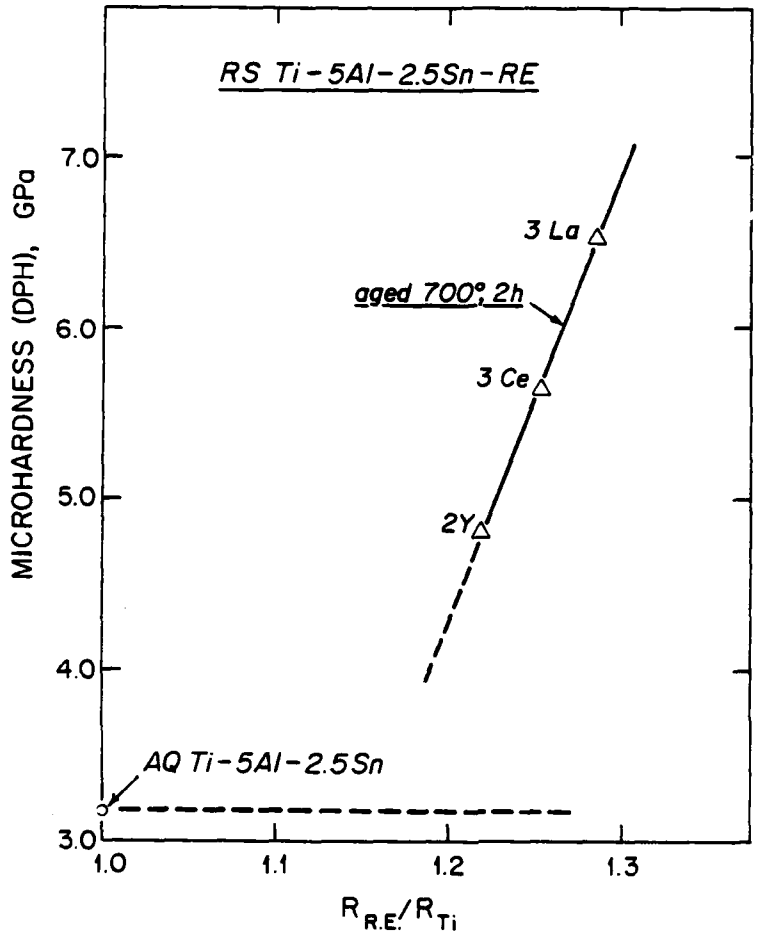

Figure 12 - Atomic size ratio vs microhardness in Ti-5-2.5-RE (RE: 2Y,3La,3Ce)

Conclusions

1. α-Ti alloys containing the group IIIA and IVA metals (Al,Sn,Ge) and rare earth metals (Y,La,Ce, etc.) form precipitate during heat treatment, which give rise to a strong age hardening.

2. The precipitate appears to take the form of a compound which exists in the phase diagram between group IIIA or IVA elements and rare earth metals from EDXS analysis.

3. Strength increase was observed in as-quenched as well as aged states. The overall increase is as much as 30-80% from that of AQ Ti-5Al-2.5Sn.

4. It is possible that for other types of Ti alloys such as near-alpha, and α/β alloys microstructure and mechanical properties can be modified by the rare earth addition discussed in this paper.

5. Strength increase in RS α-Ti alloys is a linear function of a misfit parameter, which is consistent with the previous theory.

6. Sample thickness, therefore cooling rate is a non-negligible factor affecting the strength of as-quenched and aged alloys as well.

Acknowledgements

The authors wish to express thanks for the support by the Office of Naval Research, VA (Contract No. N00014-82-K-0597). We thank Prof. J.B. Vander Sande for allowing us to use TEM facilities at MIT. Contribution #186 of the Institute of Chemical Analysis.

References

1. Proc. 2nd Int. Conf. on Rapidly Quenched Metals, N.J. Grant and B.C. Giessen, Eds., MIT press (1976); Proc. 3rd Int. Conf. on RQM, B. Cantor Ed., The Metals Society (1978); Proc. 4th Int. Conf. on RQM, T. Masumoto and K. Suzuki, the Japan Institute of Metals (1982).

2. Proc. 1st and 2nd Int. Conf. on Rapid Solidification Processing, R. Mehrabian, B.H. Kear and M. Cohen, Eds., Baton Rouge, Claitor's Publishing Dir., 1977 & 1980.

3. S.H. Whang and Y.Z. Lu, "Synthesis, Mechanical Properties and Microstructure of Novel Ti Rich Microcrystalline Alloys", paper presented at TMS-AIME Annual Meeting, Atlanta, GA, March, 1983.

4. Y.Z. Lu, S.H. Whang and Y.W. Kim, "Age Hardening of Rapidly Solidified Ti-Zr-B and Ti-Zr-Si Alloys", paper presented at TMS-AIME Fall Meeting, St. Louis, MO, October, 1982.

5. A.G. Jackson, T.F. Broderick, F.H. Froes and J. Moteff, Third Conf. on Rapid Solidification Processing, NBS, MD, December, 1982, in press.

6. P.R. Frausto, A.G. Jackson, A.H. Clauer and J.L. McCall, Microstructural Science, Vol. 10 (1982) 103-111.

7. S.M.L. Sastry, T.C. Peng, and J.E. O'Neal, 1982 TMS-AIME Meeting, October 25-28, St. Louis, MO.

8. F.E. Luborsky and J.L. Walter, J. Appl. Phys., 47 (1976) 3648-3650.

9. S.H. Whang and Y.Z. Lu, "Aging Behavior of Devitrified Ti Rich Alloys Containing Metalloids", Proc. Third Rapid Solidification Processing, NBS, MD, December, 1982, in press.

10. R.C. Ruhl, Mat. Sci. & Eng. 1 (1976) 312.

11. C.S. Chi and S.H. Whant, "High Temperatures α-Ti Alloys Containing Rare Earth Metals via Rapid Solidification Processing", in preparation, to be submitted to J. Mat. Sci.

12. F.R.N. Nabarro, Proc. Soc. 58 (1946) 669.

13. A.H. Cottrell, "Dislocations and Plastic Flow in Crystals", Oxford (1953) 125.

14. N.P. Allen, T.H. Schofield, and A.E.L. Tate, Nature, 168 (1951) 378.

15. P. Farrer in Proc. 3rd Int. Conf. on Strength of Metals and Alloys, the Metals Society, London, Vol. 1 (1973) 46.

AGING BEHAVIOR OF DEVITRIFIED Ti RICH ALLOYS CONTAINING METALLOIDS

S. H. Whang and Y. Z. Lu

Northeastern University
Boston, MA 02115

AGING BEHAVIOR OF DEVITRIFIED Ti RICH ALLOYS CONTAINING METALLOIDS

Sung H. Whang and Y.Z. Lu

NORTHEASTERN UNIVERSITY
Boston, MA 02115

ABSTRACT

Rapidly quenched Ti rich glassy alloys containing B and Si were made and devitrified as functions of temperature (550 - 950°C) and time. Different aging responses for $Ti_{70}Zr_{10}Ni_{10}B_{10}$ and $Ti_{70}Zr_{10}Ni_{10}Si_{10}$ were observed from the annealing experiments. For the former, initial modest aging response was followed by a strong second response after a long-hour annealing at 700°C while for the latter the first response only was detected. Also, the second aging in the Ti-Zr-Ni-B alloy develops very high hardness as well as a brittle phase.

Microstructure of heat treated $Ti_{68}Zr_6Al_4Ni_{10}B_{12}$ glass at 950°C for 2 hours shows that grain size remains within sub-micron range in diameter while precipitate grows into a half-micron size of acicular shape.

Introduction

Recently, a unique microstructure exhibiting high hot and cold strength has been synthesized via devitrification of glassy alloys containing metalloids [1][2][3]. Particularly, this group of alloys, in which sub-micron equiaxed metalloid dispersoid and metalloid-insoluble metal matrix form a network structure, gives rise to a microstructure stable at high temperature with unique mechanical properties. Similarly, a large quantity of metalloid elements (~up to 20 at %) can be dissolved in Ti alloys via glass formation and later precipitated out by annealing. The following is a preliminary study of devitrified microstructure and mechanical properties of Ti rich glasses.

Experimental

An alloy button prepared in an arc furnace under inert gas atmosphere was splat-quenched using hammer and anvil technique. The sample foils were examined by x-ray diffractometer to determine amorphousness. Subsequently, the crystallization of the glassy alloy was studied by DSC-2 calorimetry with a heating rate of 80 K/min and a temperature range up to 1000 K. To study aging behavior the samples were wrapped in thin tantalum foil and sealed in quartz capsules under vacuum (10^{-3} torr) the capsules samples were heat treated in a furnace as functions of temperature and time. Hardness of the samples was measured by Vickers diamond pyramid tester using 50 and 100 g loads.

Results

a) Glassy State

Table 1 shows measured hardness (Hv) and crystallization temperatures (Tx) for some Ti-Zr-M-B (Si) alloys and as-quenched Ti-6Al-4V alloy, where M is Cr, Mo, Ni and Al. Young's modulus was estimated from a correlation between hardness and Young's modulus in glassy alloy [4]. Each alloy has more than one exotherm. The temperature at which the strongest peak occurs was indicated with an

Table 1

Properties of Ti-Rich Glassy Alloys Before and After Crystallization

Alloy	As-Quenched Structure	Microhardness Hv (GPa)	Estimated Young's Modulus (E) (GPa)	Crystallization Temperature (°C)	Aged; 750°C 2h, Hv (GPa)
$Ti_{70}Zr_{10}Ni_{10}B_{10}$	Glass	6.31 (G)	~115	357,452	9.7
$Ti_{68}Zr_6Al_4Ni_{10}B_{12}$	Glass	6.27 (G)	~114	407,477	9.6
$Ti_{70}Zr_{10}Ni_{10}Si_{10}$	Glass	4.94 (G)	~87	413,544*	8.8
$Ti_{70}Zr_{10}Mo_2Cr_4Ni_4Si_{10}$	Glass	5.83 (G)	~106	419,551*,567	6.2
Ti-6Al-4V	Cryst.	4.28 (C)			

*Major exotherm

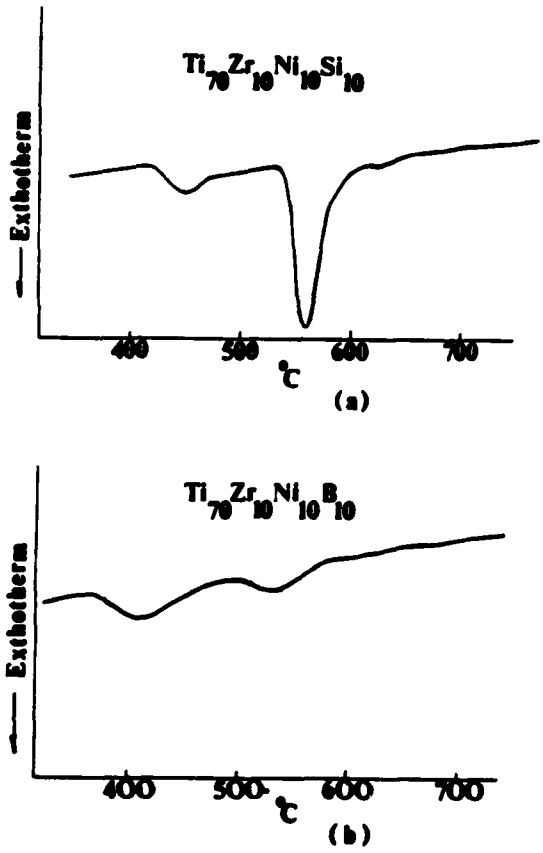

Figs. 1(a) and 1(b) One of two exotherms for the Ti-Zr-Ni-Si (a) is very strong in contrast with two weak peaks in the Ti-Zr-Ni-B (b).

asterisk in the table. It is interesting to note that $Ti_{70}Zr_{10}Ni_{10}B_{10}$ does not exhibit any strong exothermal peak as shown in Fig. 1(b). The crystallization temperatures of $Ti_{70}Zr_{10}Ni_{10}Si_{10}$ are similar to those of $Ti_{70}Ni_{20}Si_{10}$ glass (426°C, 539°C) [5]. The Ti alloys containing B show higher hardness in both glassy and crystalline states than the Ti alloys with Si. Overall, hardness values at aged state are as much as 10 - 80% higher than those at glassy state.

b) Heat Treatment

As-quenched glassy alloys were crystallized isochronally at a temperature range of 550 - 950°C for 2 hours. Measured hardness for $Ti_{70}Zr_{10}Ni_{10}Si_{10}$ and $Ti_{70}Zr_{10}Ni_{10}B_{10}$ alloys was plotted against annealing temperature as shown in Fig. 2. For both alloys lower temperature annealing gives rise to higher strength than higher temperature annealing, which is expected from the growth kinetics of grain and precipitate. The fact that in $Ti_{70}Zr_{10}Ni_{10}B_{10}$ hardness does not change in the range of 750 - 950°C may be indicative of insignificant microstructural change above 750°C. Isothermal annealing was conducted on $Ti_{70}Zr_{10}Ni_{10}B_{10}$ and $Ti_{70}Zr_{10}Ni_{10}Si_{10}$ at 700°C below β transus shown in Fig. 3. Initial aging response presumably comes from α-Ti and titanium-metalloid compound. However, the second aging response for the Ti-Zr-Ni-B alloy occurs after ten hour annealing. Also, it is interesting to point out that similar double aging was observed in $Ti_{90-x}Zr_{10}B_x$ but not in $Ti_{90-x}Zr_{10}Si_x$, where x = 1-8 [6].

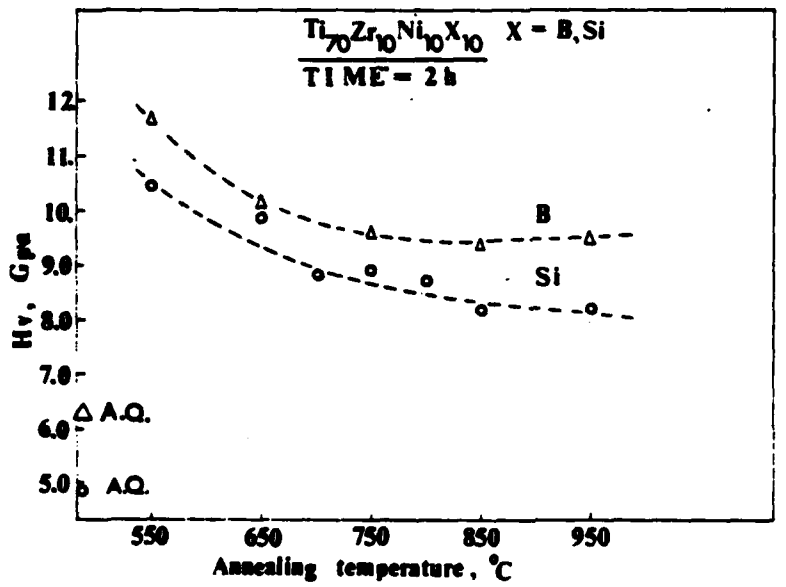

Fig. 2 Isochronal annealing (2h) at a temperature range of 550°C - 950°C for $Ti_{70}Zr_{10}Ni_{10}B_{10}$ and $Ti_{70}Zr_{10}Ni_{10}Si_{10}$.

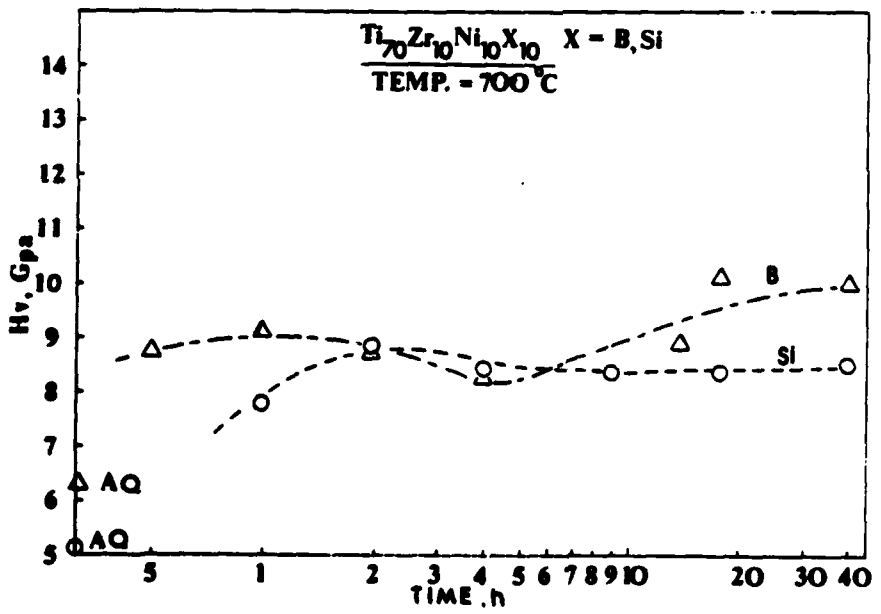

Fig. 3 Isothermal annealing at 700°C at a range of 0.5 - 40 h for $Ti_{70}Zr_{10}Ni_{10}B_{10}$ and $Ti_{70}Zr_{10}Ni_{10}Si_{10}$.

Microstructure

Bright field TEM micrograph of $Ti_{68}Zr_6Al_4Ni_{10}B_{12}$ alloy aged at 550°C for 4 hours shown in Fig. 4(a) exhibits very fine early stage crystallization and grain growth. The corresponding diffraction pattern shown in Fig. 4(b) also confirms the fact that grain size is indeed very small from the continuous first debye ring. A number of bright spots inside the first ring indicate the existance of precipitates having a larger cell size, probably borides.

In Figs. 5(a) and 5(b), microstructure of the Ti-Zr-Al-Ni-B alloy annealed at 950°C for 2 hours exhibits sub-micron grains and randomly scattered needle shape precipitates. From these micrographs grain growth in the devitrified Ti alloy is not serious even at the elevated temperature and the grain size remains within a sub-micron range while precipitate grows large enough to alter mechanical properties of the alloy.

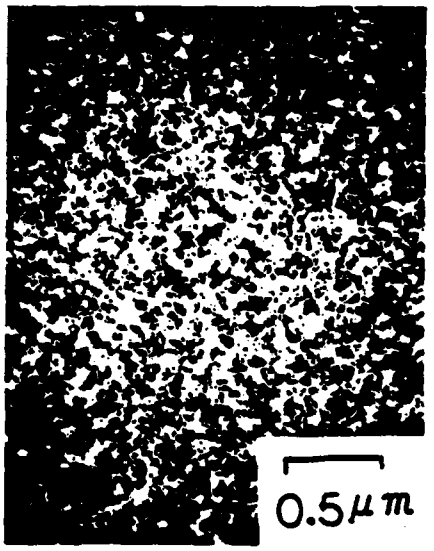

Fig. 4(a) Electron Micrograph of $Ti_{68}Zr_6Al_4Ni_{10}B_{12}$ aged at 550°C for 4 hours.

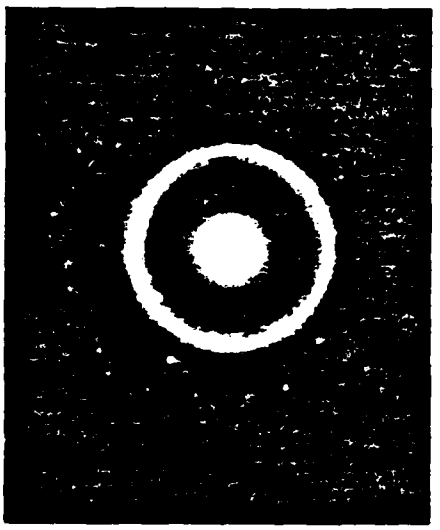

Fig. 4(b) Diffraction pattern of 4(a).

Fig. 5(a) Micrograph of the Ti-Zr-Al-Ni-B alloy annealed at 950°C for 2 hours.

Fig. 5(b) Higher magnification micrograph of 5(a).

Discussions

Glass forming ability of Ti alloy containing Si is superior to that of Ti alloy containing B. For example, glass forming was observed in binary Ti-Si but not in binary Ti-B. Also, $Ti_{74}Zr_{10}Ni_6Si_{10}$ alloy forms glass upon quenching while $Ti_{80-x}Zr_{10}Ni_xB_{10}$ alloys require full 10% Ni to go to glassy state.

It is speculated that precipitate reaction corresponding to the second aging response shown in the isothermal annealing of the Ti-Zr-Ni-B alloy may not be shown in the DSC-pattern as well as in the isochronal plot probably because of its high temperature and sluggish kinetics. The reason for the double aging in the Ti-Zr-Ni-B alloy may be as follows. For the initial age hardening, orthorhombic TiB or unknown (Ti, Zr)B type may be formed (based on phase diagram information). At the same time, the formation of hexagonal ZrB_2 or perhaps $(Zr, Ti)B_2$ can be possible thermodynamically although nucleation and growth of this compound may be sluggish. Therefore, the second aging is believed to be associated with the precipitation of this compound. On the other hand, single aging response for the Ti-Zr-Ni-Si alloy is consistent with that for Ti-5Zr-1Si [7], in which $(Ti, Zr)_5Si_3$ was identified as a G.P. zone precipitate instead of Ti_5Si_3. The devitrified Ti alloys in this experiment are brittle except the Ti-Zr-Mo-Ni-Si. Furthermore, extensive brittleness develops in these alloys after long time annealing at a higher temperature. This is coincident with the microstructure of the annealed Ti-Zr-Al-Ni-B alloy in which acicular shape precipitates were found. However, for the Ti-Zr-Mo-Cr-Ni-Si alloy, a significant portion of ductility remains after devitrification and annealing at higher temperature (700 - 1000°C).

Acknowledgements

The authors wish to thank Mr. G. Mouchawar and K. Carlson for their assistance in carrying out this experiment. This work has been supported by the Office of Naval Research, Arlington, VA, which is gratefully acknowledged.

References

[1] Ranjan Ray, J. Mat. Sci., 16 (1981) 2924.

[2] Ranjan Ray, Proc. Mat. Res. Conf., Rapidly Solidified Amorphous and Crystalline Alloys, B.H. Kear, B.C. Giessen and M. Cohen, eds., 8 (1981) 435.

[3] C.C. Wan, Proc. Mat. Res. Conf., Rapidly Solidified Amorphous and Crystalline Alloys, B.H. Kear, B.C. Giessen and M. Cohen, eds., 8 (1981) 441.

[4] S.H. Whang, D.E. Polk and B.C. Giessen, Proc. 4th Int. Conf. on Rapidly Quenched Metals, Sendai Japan (1981) 1365.

[5] D.E. Polk, A. Calka and B.C. Giessen, Acta Met., 26 (1978) 1097.

[6] Y.Z. Lu and Sung H. Whang, TMS-AIME Fall 1982, St. Louis, MO, to be published.

[7] H.M. Flower, P.R. Swann and D.R.F. West, Titanium Science and Technology, eds., Jaffee & Burte, 2 (1972) 1143.

GLASS FORMING ABILITY FOR BINARY ALLOY SYSTEMS BY MODIFIED T-C MAP IN RELATION TO PHASE DIAGRAM

S. H. Whang

Northeastern University
Boston, MA 02115

Fifth Int. Conf. Liquid and Amorphous Metals, Aug. 15-19,1983
UCLA, Calif. To be published in J. Non-Cryst. Solids.

GLASS FORMING ABILITY FOR BINARY ALLOY SYSTEMS BY MODIFIED T-C MAP IN RELATION TO PHASE DIAGRAM

S. H. WHANG*

Materials Science Division, Institute of Chemical Analysis, Northeastern University, Boston, MA 02115

In order to make a more accurate prediction for glass forming ability (GFA) of alloy systems, the temperature-composition map was further modified by considering kinetic aspects of solidification. Glass forming ability as well as compositional range (GFCR) for Cu, Ag and Au rich binary alloys were studied using the modified model. All predictions are in good agreement with experimental observations. It is shown that GFA of eutectics depends on the local morphology of the liquidus curve and the melting points of the base phases involved.

1. INTRODUCTION

Search for glass forming compositions has been conducted near eutectics in alloy phase diagram since an abnormally deep eutectic is considered as the most probable site for glass formation.[1] In fact, experimental results show that the high value of reduced glass transition temperature, T_{gr} occurs near the eutectic. However, at present, since it is not possible to predict glass transition temperature by ab initio calculation, other approaches have been taken that use indirect parameters with different origins in order to predict GFA as well as GFCR. These parameters include reduced liquidus temperature, degree of undercooling, viscosity, atomic size ratio, electronegativity difference, heat of formation for liquid metals, valence electron concentration, type of intermetallic compound, etc. Intially, these parameters are employed individually to identify GFA, which is reviewed elsewhere.[2]

The methodology used for the prediction may be divided into two categories. They are: 1) to distinguish ready glass formers from non-ready glass formers based on thermodynamic principles, in particular utilizing phase diagram features; 2) to predict GFA based on correlations between fundamental parameters and GFA. In the first category, the first systematic step toward the prediction of GFA was made using reduced liquidus temperature based on ideal solid solution theory.[3] The prediction by this model is limited to those eutectics without terminal solid solution. Subsequently, for more broad application, the mixture

*Sponsored by the Office of Naval Research, Contract N00014-82-K-0597

of the melting points of the two pure components, $\bar{T}_L^o$ as the reference liquidus temperature was proposed.[4] Such schemes for GFA prediction were seriously challenged when applied to binary Ti alloys where terminal solid solution is pronounced. Based on empirical observation, an additional parameter so called reduced eutectic composition, C_{ER} was introduced to construct 2-D map together with the reduced liquidus temperature, T_{LR} in order to take into account the effect of the excess stability of the solid solution on GFA.[5]

On the other hand, GFAs of various binary alloy systems were predicted in the 2-D map of heat of formation for liquid metals and atomic radius ratio of the two components without the aid of phase diagram.[6] This approach is similar to the Darken-Gurry plots[7] and Chelikowsky map[8] in which the types of solid solution was successfully predicted in 2-D maps.

It is shown that in general the predictability is improved drastically when two different parameters with different origins are employed in a 2-D map. Presently, a new approach using multi-parameters to identify GFA and GFCR based on pattern recognition method is under study.[9]

2. TEMPERATURE-COMPOSITION MAP (T-C MAP)

Previously, from the relationship between linear T_o and nearly constant T_g, the following approximation was derived:[5]

$$\frac{\Delta T_M}{T_E}\left(\frac{2}{2-C_{ER}} - 1\right) = K \quad \text{for } 0 < C_{ER} \leq 1 \qquad (1)$$

$$\simeq T_{LR} \cdot \left(\frac{2}{2-C_{ER}} - 1\right) \quad \text{if } \Delta T_M \ll T_E \ \& \ T_M^A \simeq T_M^B$$

Where $\Delta T_M = T_M^A - T_E$; $T_{LR} = (\bar{T}_L^o - T_L)/\bar{T}_L^o$; and $C_{ER} = (C_E - C_s)/C_E$

T_M^A is melting temperature of component A; T_E is eutectic temperature, T_L is the liquidus temperature; C_s is solid solubility at the eutectic temperature; C_E is eutectic composition; K is constant determined from the T-C map. In particular, in the original T-C model, the liquidus depression of those eutectics associated with compound phases was measured with $\bar{T}_L^o$ by neglecting the related compound phases. By considering many similarities that exist between the terminal pure component phases and the intermetallic compounds such as $T_o/T_M = 1$, stoichiometric compositions, relatively sharp free energy curves, etc., tentatively those compound phases will be treated as terminal pure components in this model. As a result, each phase diagram can be divided into many "sub" phase diagrams that can be dealt with independently for GFA. In the following, the detailed aspects of the modified model will be explained with sample phase diagrams:

Example 1: If an alloy system either possesses only one eutectic or many intermetallic compounds that can be easily suppressed during quenching and therefore can be treated as a single eutectic system, $\bar{T}_L^o$ can be used as the reference temperature. A good example is Zr-Cu system shown in Fig. 1, in which the intermetallic compounds existing at intermediate range have low melting temperatures as well as being not kinetically active upon quenching. Predicted and experimental values for GFCR are in excellent agreement.

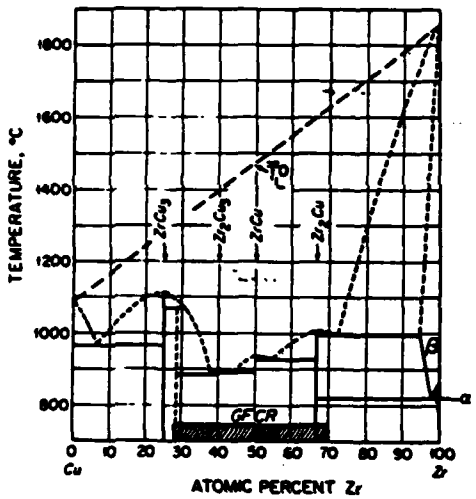

FIGURE 1
A tie line between the melting points of Zr and Cu as the reference liquidus temperature

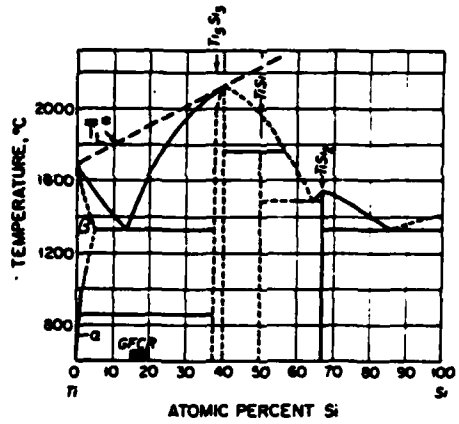

FIGURE 2
The reference liquidus line, $\bar{T}_L^*$ between the melting points of Ti and Ti_5Si_3

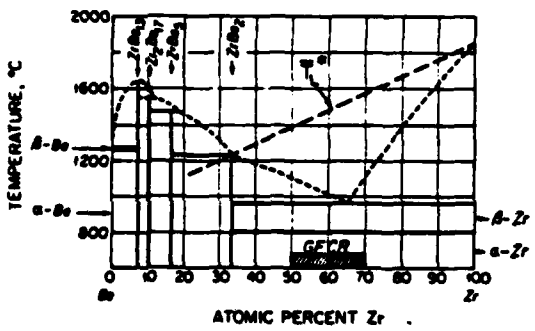

FIGURE 3
The reference liquidus line was drawn between the melting temperatures of Zr and $ZrBe_2$

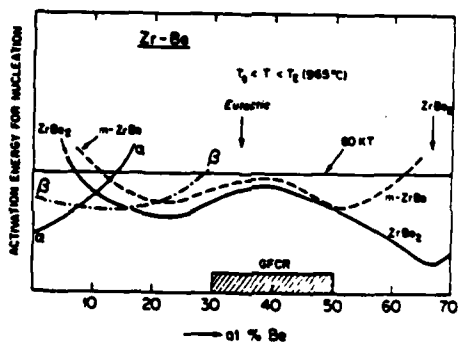

FIGURE 4
Hypothetical nucleation situation of undercooled melt at a temperature between $T_g < T < T_E$

Example 2: If the melting temperature of an intermetallic compound T_M^* is much higher than $\bar{T}_L^o$, the compound may be too stable thermodynamically as well as kinetically to be suppressed upon rapid quenching. In that case, obviously, sub-phase diagram approach should be taken. In Figure 2, the sub-phase diagram

was constructed by Ti and Ti_5Si_3 phases. The corresponding reference temperature is T_L^* as indicated in the Figure. The prediction for GFCR is consistent with the experimental results.

Example 3: For those compounds that have low melting temperature, but the crystallization can't be prevented for a given quenching rate, the sub-phase diagram approach provides better results for GFCR. An example is shown in Figure 3 and the corresponding hypothetical nucleation situation is shown in Figure 4 referring to TEM observation.[10]

3. BINARY ALLOY SYSTEMS

3.1 GFA of eutectic alloy

GFA of eutectic compositions for Ti,Zr,Si and Al alloy systems have been reported.[5] In this paper, some of the eutectic alloys in Cu,Ag, and Au rich binary systems were investigated using the T-C maps. All alloy samples were melted and quenched in an arc melting furnace using the hammer and anvil technique. A majority of samples were ∿25μm thick and believed to be

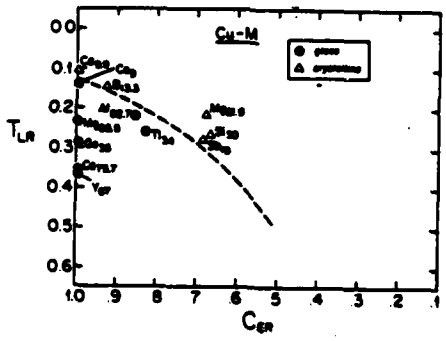

FIGURE 5
Predicted ready glass formation for eutectic alloys of Cu-M systems by T-C map

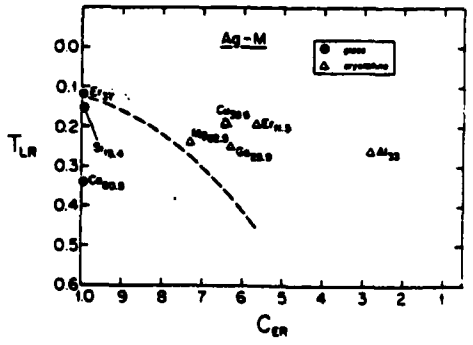

FIGURE 6
Predicted RGF for eutectic alloys of Ag-M systems

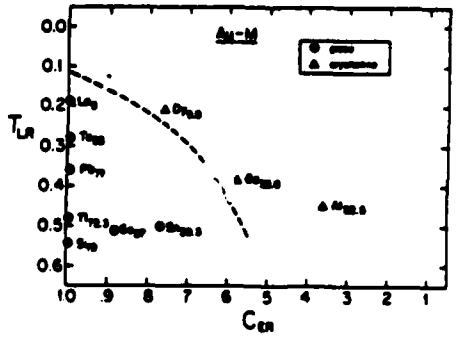

FIGURE 7
Predicted RGF for eutectic alloys of Au-M systems

quenched at the cooling rate of $\sim 10^6$K/sec. Figs. 5, 6 and 7 present the GFA of eutectic alloys for Cu,Ag and Au rich binary systems respectively. A good separation between the ready glass former (RGF) and non-RGF was observed for all alloy systems. One particular case is $Cu_{70}Si_{30}$ which is supposedly a good glass former according to the initial T-C model. Now, considering the solubility of intermetallic phase, $Cu_{70}Si_{30}$ becomes a non-easy glass former in the map with C_{ER} value of 0.66.

3.2 Glass forming compositional range (GFCR)

GFA models based on phase diagram have an advantage over other models in that precise glass forming compositions can be predicted in binary alloy systems. Although previously accurate prediction of GFCR by the original T-C model for many binary alloys have been demonstrated, GFCR was exaggerated for some alloy systems. The modified T-C model resolved such an inconsistency of the previous model. Those alloys are shown in Table 1. For Ti-Ni,Ti-Si,Ag-Ca and Au-Ca, precise prediction for GFCR is possible by the modified model. For the rest of the alloys, a significant improvement was made by the new model.

TABLE 1. GLASS FORMING COMPOSITIONAL RANGE FOR BINARY ALLOY

Alloy	Exp.	Original T-C Model	Modified T-C Model	Compound Structure
Ag-Ca	60-85(Ca)	9-90(Ca)	62-87(Ca)	CaAg (fcc,Al)
Au-Ca	72.5-88.7(Ca)	82-88(Ca)	72-89(Ca)	$Ca_{10}Au_9$
Au-Sn	29-$\sim$35(Sn)	13-90(Sn)	20-44(Sn)	AuSn (NiAs,$B8_1$)
Fe-B	13-27(B)	8-42(B)	8-30(B)	FeB (Orth.Rh. B27)
Ti-Ni	25-40(Ni)	11-68(Ni)	25-39(Ni)	TiNi (CsCl,B2)
Ti-Si	15-20(Si)	13-14(Si)	15-21(Si)	Ti_5Si_3 (Mn_5Si_3,$D8_8$)
Zr-Be	30-50(Be)	15-72(Be)	16-55(Be)	$ZrBe_2$ (AlB_2,C32)
Zr-Pt	$\sim$20-$\sim$40(pt)	12-28(pt)	11-34(pt)	PtZr(CsCl,B2)
Zr-Si	13-22(Si)	9-10(Si)	10-18(Si)	Zr_5Si_3(Mn_5Si_3,$D8_8$)

5. DISCUSSIONS

For Cu,Ag and Au rich alloy systems, the T-C map systematically deviates from the standard map.[5] In other words, T_{LR} value along the RGF boundary curve increases more rapidly in these alloy systems than in the standard map. Therefore, K in eq (1) appears to be no longer constant. Such a deviation may be understood from the fact that the T_o line at hypoeutectic side is concave upward. However, it is not because the disagreement between $\Delta T_M/T_E$ and T_{LR} becomes larger with decreasing T_E. An example may be found in Ag-Cu system in which solid solution can be stabilized over the entire compositional range by rapid quenching.[11]

GFCR prediction was greatly improved by the modified T-C model. However, systematic information that identifies GFA of intermetallic compound phase has not been available. From Table 1, it is noticed that the majority of kinetically active compounds occurs at 50-50 composition. Also it is interesting to see that a third dimension such as normalized quantity $T_n/\dot{T}^{12}$ or $\Delta T/\dot{T}$ is added to the T-C map, where $\dot{T}$ is cooling rate. Currently, a lack of data in this area would be a major stumbling block in incorporating such a kinetic parameter with the T-C map.

Finally, equilibrium phase diagram does not represent the kinetic behavior of super-cooled liquidus metals. Instead, metastable phase diagram would be a great help in understanding the kinetics of intermetallic compound phase upon quenching and thereby predicting the GFA of the entire phase diagram.

ACKNOWLEDGEMENT

The author thanks Prof. B. C. Giessen for his encouragement for this work. The author also is indebted to Ms D. M. Kao and Mr. Y. Z. Lu for their assistance in the experiments. Contribution #180 of the Institute of Chemical Analysis

REFERENCES

1) David Turnbull, Contemp. Phys. 10 (1969) 473-488.

2) D. E. Polk and B. C. Giessen, Metallic Glasses, American Society for Metals, Metals Park, OH 1978.

3) M. Marcus and D. Turnbull, Mat. Sci. Eng., 23 (1976) 211-214.

4) I. W. Donald and H. A. Davies, J. Non-Cryst. Solids, 30 (1978) 77-85.

5) S. H. Whang, Mat. Sci. Eng. 57 (1983) 87-95.

6) B. C. Giessen and S. H. Whang, Journal DePhysique Colloque C8 (1980) C8-95.

7) L. S. Darken and R. W. Gurry, Physical Chemistry of Metals (McGraw-Hill, New York 1953) 74.

8) J. R. Chelikowsky, Phys. Rev. B, 19 (1979) 686.

9) B. C. Giessen and Y. Q. Gao, see the proc. of this Conference.

10) L. E. Tanner and R. Ray, Acta. Met., 27 (1979) 1727.

11) P. Duwez, R. H. Willens and W. Klement, J. Appl. Phys. 31 (1960) 1136.

12) T. B. Massalski, C. G. Woychik and J. L. Murray, Proc. MRS Sym., Alloy Phase Diagram, L. H. Bennett, T. B. Massalski and B. C. Giessen, eds. (1983) 241.

GLASS FORMING PROPERTY OF Ti-Zr-Si SYSTEM DETERMINED BY TEMPERATURE-COMPOSITION MAP

S. H. Whang

Northeastern University
Boston, MA 02115

Submitted to Scripta Met.

GLASS FORMING PROPERTY OF A Ti-Zr-Si SYSTEM DETERMINED BY TEMPERATURE-COMPOSITION MAP

S. H. WHANG
Barnett Institute of Chemical Analysis and Materials Science
Northeastern University
Boston, Massachusetts 02115

INTRODUCTION

The glass forming ability (GFA) of numerous alloy systems has been a subject of study by many scientists in the last two decades. As a result, a number of models have emerged that can be used for the prediction of the GFA of binary alloy systems. All these models have foundations on semi-empiricalism while ab initio calculation from the first principle has not yet been developed. In the beginning, the glass forming ability of binary alloy systems has been studied by a single parameter, i.e., a reduced liquidus temperature that derived from a phase diagram (1,2). However, the prediction of GFA by a single parameter has not been satisfactory except for a simple phase diagram such as a mono-eutectic system without a terminal solid solubility. Recently, the use of two parameters in a two-dimensional map (2-D map) has received much attention since the separation between the ready and the non-ready glass formers becomes distinctive in this scheme. As a more fundamental approach, two parameters such as the atomic radius ratio between the solvent and solute and the heat of solution for liquid metals has been utilized in a two-dimensional map to predict ready glass forming binary alloys (3-5). Another 2-D map with two parameters, namely of the reduced liquid temperature and so called "reduced eutectic composition" (T-C map) has been employed to determine the GFA as well as compositional range in a binary alloy system (6,7). For 100 binary eutectic alloys of Ti, Zr, Al, Si (6) and Cu, Ag, Au (7) which were quenched at a cooling rate of $\sim 10^6$K/sec, the GFA has been predicted correctly by this model, which is consistent with experimental observations. In addition, the glass forming compositional ranges (GFCR) in 19 binary alloy systems identified satisfactorily by this model. The advantage of this model, based on phase diagram features, is that a precise glass forming composition can be determined. In practice, it is important to know the glass forming ability of ternary or higher order alloy system but, to date, no attempt has been made to predict the GFA for such systems. The prediction of the GFA of a ternary system requires dealing with additional problems. First, the details of the ternary phase diagrams for the majority of ternary alloy systems are not known. Secondly, no model has been known to be effective in dealing with the GFA of a ternary system. These are the subjects of discussion in this paper.

MODEL

It is well known that a large liquidus depression at the eutectic in the equilibrium phase diagram is often associated with ready glass formation upon rapid liquid quenching (8). However, when a terminal solid solution in binary systems is also present, the result is a stable extended solid solution instead of a glassy phase. Therefore, it is important to consider these two factors simultaneously in order to determine the ready glass formation of any alloy composition. Theoretically, when liquid metals cool down beyond a T_o point which is an interesting point of the two loci of the liquidus and solidus curves in the free energy-composition diagram, it is possible that the undercooled liquid transforms into a partitionless solid solution upon rapid solidification since the eutectic decomposition from the liquid phase is a very slow process (9). However, when the T_o line plunges sharply into a solid phase so that an opening between the two T_o curves near the eutectic is created, the liquid often

transforms into a glassy phase upon rapid quenching (9,10). This may be so because the glass transition only competes with the eutectic reaction at the opening. Although glass transition temperature changes monotonically as a function of composition in an alloy system, it is assumed to be a constant in this model. Accordingly, the T_o line is the only controlling parameter for determining the glass forming ability. Now, the T_o line in an alloy system is deviating from a lineality, but it is dealt as a straight line in the present model. From the simple geometrical relation in a phase diagram, the following equation may be obtained, which is described in detail elsewhere (6,7).

$$T_{LR} \cdot \left(\frac{2}{2-C_{ER}} - 1\right) \simeq K \text{ for } 0<C_{ER}<1 \quad \text{----------(1)}$$

where $T_{LR} = (\bar{T}_L^o - T_L)/\bar{T}_L^o$; $C_{ER} = (C_E - C_s)/C_E$, $\bar{T}_L^o$ = weighted average of melting points of two pure components, T_L = liquidus temperature, C_E = eutectic composition, C_s = maximum solubility at eutectic temperature

K is a constant which is determined by a boundary curve that separates the ready and non-ready glass formers in the T-C map. As has been applied successfully to binary alloy systems by the author (6,7), this model could be also employed for a ternary system if the T_{LR} and C_{ER} values can be determined. The liquidus surface of a ternary alloy system can be obtained by experiment or by computer technique. In this work, the computer technique for the calculation of phase diagram based on regular and non-regular solution model developed by Kaufman et al (11) were employed to determine the T_{LR} and C_{ER} values for a given K value in the equation (1). The K value obtained from the previous work for the binary alloy systems is ~0.1. This K value again will be adopted in this calculation. It should be mentioned that in the previous binary works, the better results for the glass forming compositional range has been obtained when $\bar{T}_L^o$ was replaced by $\bar{T}_L^*$ where $\bar{T}_L^* = ((f_B^* - f_B)/f_B^*) * T_M^A + (f_B./f_B^*) * T_M^*$: f_B^* the atomic fraction of the B type atom in the in the compound phase; f_B the atomic fractionof the B atom in the composition under consideration; T_M^A the melting temperature of the A type atom; T_M^* the melting temperature of the compound phase. In this case, the A component and the compound phase are postulated to form a "sub-phase diagram" (7). Hence in this work, this sub-phase diagram approach will be used to yield a better result. Now, the reference liquidus surface in the Ti-Zr-Si system contains the four melting temperatures of Ti_5Si_3, Zr_5Si_3, pure Ti and pure Zr. At first, two straight tie lines, i.e., one between Ti_5Si_3 and Zr_5Si_3 and the other between pure Ti and pure Zr, are drawn and as a next step, to obtain the $\bar{T}_L^*$ surface, many tie lines connecting the original two tie lines are constructed in such a way that the tie lines point to the Si vertex in the ternary phase diagram. The predicted glass forming range will be compared with that obtained by experiments in the following.

EXPERIMENTAL

The ternary alloys along the eutectic line in the Ti-Zr-Si were prepared in an arc-melt furnace and splat quenched into 20-25 μm thick foil from liquid by the hammer and anvil technique. The splat foil were examined by x-ray diffractometry to confirm their amorphousness. The cooling rate in this thickness range is estimated to be $\sim 10^6$K/sec from the Ruhl's calculation (12). The experiment continued until the glass forming compositions were mapped in this system.

RESULTS AND DISCUSSIONS

Figure 1 shows predicted glass forming compositions outlined by dashed lines while the hatched area indicates the glass forming compositions determined by experiment. The glass forming compositions can be divided into two categories: the hypoeutectic and hypereutectic domains. In the hypereutectic domain, the agreement between the experiments and the calculated results is satisfactory, but it is poor in the hypoeutectic domain. We will examine the reason for such a disagreement existing in the hypoeutectic side.

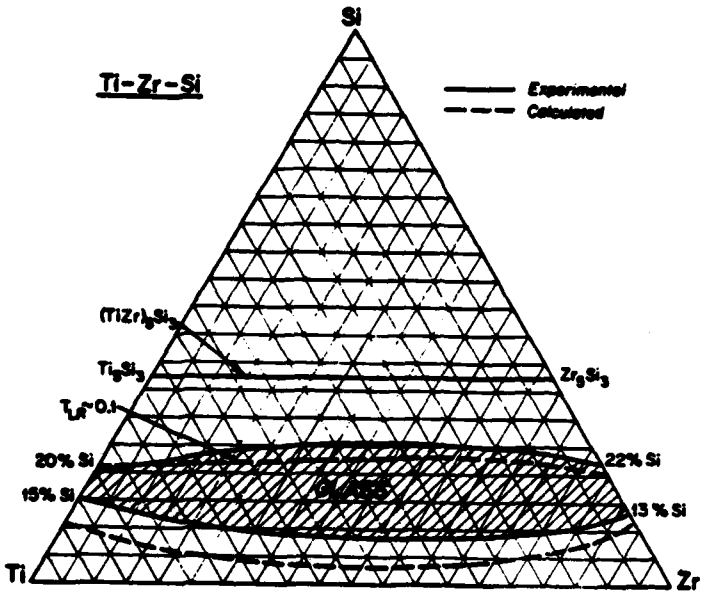

Fig. 1

Glass forming compositions in Ti-Zr-Si. The hatched area is determined by the experiment and the dashed line by this model with the aid of computer calculations.

The two possible sources of the error can be either the error in the computer-calculated phase diagram or the uncertainty involved in the model itself. Specifically, we will examine such possibilities from the two binary sides, i.e., Ti-Si and Zr-Si.

TABLE 1

Alloy	Experimental (at % Si)	T-C/E Scheme (at % Si)	T-C/C Scheme (at % Si)
Ti-Si	15-20	15-21	11-21
Zr-Si	13-22	10-18	11-20

Table 1 shows three different methods to identify glass forming compositions in the Ti-Si and Zr-Si systems. In the second column, the experimental results are listed; in the third column, the predicted values by the T-C model using the experimental phase diagram (T-C/E scheme) are shown; in the last column, the predicted values by the T-C model using the calculated phase diagram (T-C/C scheme) are shown. For the Ti-Si system, the experimental value agrees well with the result by the T-C/E scheme but does not with that by T-C/C scheme. This implies that the error comes from the computer-calculated phase diagram. On the other hand, in the Zr-Si system, the T-C/E scheme predicts a wider glass forming range in the hypoeutectic domain by 3 at % than that by the experiment. Therefore, it is concluded that in this case, the error originates from the uncertainties in the T-C

model itself. From the above observation, it is clear that the deviation of the predicted values (T-C/C) from the experimental values in the hypoeutectic domain is attributed to both the uncertainties in the model as well as the errors in the computer-calculated phase diagram. It has shown that GFCR is very sensitive to the shape of the liquid curve. Hence, one way to improve the predictability of the GFA may be to refine the sub-regular solution model in the computer program in such a manner that the calculated binary phase diagrams are nearly identical to the experimental phase diagrams. The approach taken here for the GFCR of the Ti-Zr-Si system demonstrates the feasibility of the GFA prediction in other ternary alloy systems using the T-C model and a computer technique.

It should be mentioned that the computer calculation for a ternary phase diagram from the three binary phase diagram is often unable to predict the occurrence of unknown ternary compound phases. In this case, this approach cannot predict the GFA of a composition in a ternary system.

SUMMARY

The concept of the T-C mapping, originally applied to the binary systems, can also be applied to simple ternary alloy systems. The predicted GFCR for the Ti-Zr-Si system is a good agreement with that of experiment. It is demonstrated that GFA of a ternary system can be predicted if the liquidus surface is determined by experiment or by computer calculation. It has shown that the GFCR is very sensitive to the morphology of the liquidus surface regardless of the alloy system. The only limitation of this approach is that the unpredictability of unknown ternary compounds by computer calculation leads to the construction of an erroneous liquid surface and, thereby, make an inaccurate prediction for the glass forming ability of a system.

ACKNOWLEDGEMENTS

The author gratefully acknowledges the support of the Office of the Naval Research, VA (Grant No. N00014-82-K-0597). Many thanks are due to Mr. Eric Reid for computer calculations. The author also is indebted to Mr. G. Mouchawar for his assitance. Contribution #183 of the Barnett Institute of Chemical Analysis.

REFERENCES

1. M. Marcus and D. Turnbull, Mat. Sci. Eng., 23, 211-214 (1976).
2. I.W. Donald and H.A. Davies, J. Non-Cryst. Solids, 30, 77-85 (1978).
3. B.C. Giessen and S.H. Whang, Proc. Fourth Int. Conf. Liquid and Amorphous Metals (LAM), J. Phys. (Paris) Colloq. C8, Supplement C8-95 (1980).
4. B.C. Giessen, Proc. Fourth Int. Conf. on Rapidly Quenched Metals (RQM), T. Masumoto and K. Suzuki Eds., 1, 213-216 (1981).
5. B.C. Giessen and S.H. Whang, Proc. Mater. Res. Soc. Sym., Boston, MA, 19, 289-294 (1982).
6. S.H. Whang, Mater. Sci. Eng., 57, 87-91 (1983).
7. S.H. Whang, Proc. 5th Int. Conf. on LAM, Aug., 1983, UCLA, CA, to be published in J. Non-Cryst. Solids (special issue), in press.
8. David Turnbull, Contemp. Phys., 10, 473-488 (1969).
9. W.J. Boettinger, F.S. Biancaniello, G.M. Kalonji and J.W. Cahn, Proc. 2nd Conf. on Rapid Solidification Processing, R. Mehrabian, B.H. Kear and M. Cohen, Eds., 50-55 (1980).
10. T.B. Massalski, Proc. 4th Int. Conf. on Rapidly Quenched Metals (RQM), T. Masumoto and K. Suzuki, Eds., 1, 203-208 (1981).
11. L. Kaufman and H. Bernstein, Computer Calculation of Phase Diagrams, Academic Press (1970); L. Kaufman and H. Nesor, Titanium Science and Technology, R.I. Jaffe and H. Burte, Eds., Plenum Press, New York, 2, 773-800 (1973); L. Kaufman, CALPHAD, 3, 45-76 (1979).
12. R.C. Ruhl, Mater. Sci. Eng., 1, 313 (1967).

METALLIC GLASS FORMATION DIAGRAMS

B. C. Giessen and S. H. Whang

Northeastern University
Boston, MA 02115

METALLIC GLASS FORMATION DIAGRAMS*

B. C. Giessen and S. H. Whang
Materials Science Division, Institute of Chemical Analysis and Department of Chemistry, Northeastern University, Boston, Massachusetts 02115 USA

ABSTRACT

The ability to predict ready glass formation (RGF) in binary alloy systems upon rapid cooling of the melt is of value both theoretically and practically. Two-dimensional maps show promise as a means of associating RGF with two system parameters which must have a combination of favorable values. In this paper, two types of glass formation diagrams are reviewed. One of these, the ΔH-r/R plot, is based on fundamental parameters which can, in principle, be derived from elemental quantities for each binary alloy system. The second type of diagram, the temperature-composition map, uses two equilibrium phase diagram features, namely reduced liquidus temperatures and reduced eutectic compositions to predict RGF. Both approaches are compared for binary alloys of Zr. The temperature-composition plot approach can be extended to predict qualitatively the RGF *composition range* of a given alloy system.

While the first metallic glass alloy to be prepared by rapid solidification processing (RSP) of the melt, Au-Si, was essentially discovered by serendipity, [1] the search for further alloy compositions capable of ready glass formation (RGF) was guided mostly by consideration of phase diagram features such as relatively low melting points and absence of competing intermetallics (both conditions being met especially at eutectic compositions). [2]

As the number of metallic glasses prepared by RSP grew, it became possible to search for better schemes to predict RGF. Metallic glasses have now been prepared in over 100 binary systems representing metals from all groups of the periodic table, and this large body of experimental data allows a better evaluation of the principles to be considered in order to predict RGF. These approaches have been catalogued previously. [3-5] It may be mentioned parenthetically that they include phase diagram related features besides those mentioned above, such as the structures of the intermetallic phases present in an alloy system. [6,7] In most of these theories on RGF, each factor, e.g., the alloy valence electron concentration or the component size ratio, is evaluated separately from other factors rather than in combination with them. It was found that each of these criteria is applicable only to certain alloy systems.

In the following we present a comparison of two recently published methods for predicting RGF in a given binary system. RGF is defined here as the ability of an alloy to be retained as a glass upon rapid quenching at cooling rates of $<10^5$-10^6 K/sec., i.e., at the cooling rates thought to be associated with melt spinning under standard conditions. [8]

Both methods described involve two-parameter plots, as suggested by the observation that no single factor seems sufficient to characterize RGF ability.

*Communication #163 of the Institute of Chemical Analysis at Northeastern University, Boston, Massachusetts 02115 USA.

Mat. Res. Soc. Symp. Proc. Vol. 19 (1983)

satisfactorily. This is analogous to the situation concerning rules for the formation of compounds or solid solutions which also require two factors to be simultaneously favorable, e.g., the Darken-Gurry plots for solid solution formation [9] or Bennett and Watson's plots for compound formation. [10] For the present case of RGF, i.e., a non-equilibrium process, the plots are a function of one or more external processing parameter(s), such as the effective cooling rate employed in quenching, presence of nucleation sites, etc.; if such parameter(s) are kept constant, a type of phase diagram results, which could be extended into three dimensions if, e.g., variable cooling rates were employed.

THE ΔH_m-r/R PLOTS

These plots were first reported by us in 1980 [5] and presented more comprehensively by one of us (BCG). [11] They are based on the premise that RGF alloys must simultaneously satisfy the requirements of a favorable negative heat of mixing, ΔH_m, and the component radius ratio, r/R, where r and R are the twelve-coordinated Goldschmidt radii of the smaller and larger component, respectively. An application of these principles to classify RGF and non-RGF in alloys of Ni is shown in Fig. 1, where the alloying partners of Ni showing RGF are seen to lie in the lower left portion of the ΔH_m-r/R plot "southwest" of the solid line while the alloys showing non-RGF lie in the remaining part of the diagram. Crudely, negative values of ΔH_m <-3 to -5 Kcal/mole and size ratios r/R $\leq$0.86 are required; however, there is an interrelationship of the critical ΔH_m and r/R values such that size ratios closer to unity require a more negative ΔH_m for RGF than is required for systems with a more "favorable" (smaller) size ratio.

An additional example of a ΔH_m-r/R plot is given for alloys of Zr, Zr-M, in Fig. 2; again it is seen that there is good separation between alloys with RGF and non-RGF. This is seen especially well by following the dashed lines in the plot which connect Zr alloys containing elements of the first long period and second/third long period, respectively. As discussed before, it is obvious from the definition of RGF used in this paper that the location of the contour line separating the regions depends on the cooling rate employed; at higher cooling rates, the line moves further out toward the top and the right side of the diagram. This effect is especially well seen for the elements of the first long period, where the transition between RGF and non-RGF (as observed in our experiments) occurs between Zr-Mn and Zr-Cr; however, while Zr-Cr is not RGF in the sense of the present definition, a Zr-Cr glass can still be made by using a quenching technique producing a higher cooling rate; the next alloy system in this sequence, Zr-V, is only incompletely glass forming and Zr-Ti does not form a glass.

In Fig. 2, triangles mark alloy systems that had not yet been investigated at the time the map was first drawn. [11] It is indicative of its predictive character that the system Zr-Si which was originally given by a triangle, [11] has since been found to be RGF, as announced at the same conference at which this diagram was presented: Zr-Si is now marked as RGF. [12]

Other alloy systems, such as those based on Ti, Nb, and Cu, have boundaries separating RGF and non-RGF regions that are similar to those for the Ni and Zr containing systems; for Pd these boundaries lie at somewhat lower ΔH_m values. [11]

TEMPERATURE-COMPOSITION MAPS

An alternative approach has been taken by one of us (SHW) in constructing maps based on equilibrium phase diagram features of the alloy system in question. [13] These maps are based on the assumption that RGF in a binary

system requires the presence of two factors: a) A sufficiently large melting point depression, as measured by the depression of the liquidus temperature T_L from an appropriately chosen melting temperature average $\overline{T}_L^o$, e.g. an average based on the component melting points T_M^A and T_M^B; $\overline{T}_L^o = X_A T_M^A + X_B T_M^B$, where X_A and X_B are the component concentrations. This melting point difference is then normalized by $\overline{T}_L^o$, leading to the normalized liquidus depression $T_{LR} = (\overline{T}_L^o - T_L)/\overline{T}_L^o$ as a convenient measure of melting point depression. b) A sufficiently low tendency for terminal solid solution (s.s.) formation, as expressed by a sufficiently large excess of the composition considered for maximum glass forming ability, e.g., the eutectic C_e, over the maximum concentration of solute in the terminal s.s. range, C_s. Again, the appropriate difference $C_e - C_s$ is normalized, this time by C_e; this leads to a reduced eutectic composition $C_{er} = (C_e - C_s)/C_e$, with increasing values of C_{er} expressing the increasing absence of the formation of s.s. which could compete with RGF at the eutectic composition upon supercooling of the alloy.

The T-C map constructed for Zr alloys based on these concepts is shown in Fig. 3; it is seen that there is good separation of RGF and non-RGF alloys in this map. (In the plot, Fig. 3, RGF and non-RGF are marked as easy glass former and non-easy glass former, respectively.) It is further seen that the agreement between the data in this plot and those in the ΔH_m-r/R plot, Fig. 2, is quite good. However, there is some disagreement for alloys marked as marginal glass formers in the ΔH_m-r/R plot such as Zr-Cr and Zr-V; the data points for these systems fall into the easy glass forming region of the T-C plot, Fig. 3. This apparent conflict can be partially resolved by assuming that the contour line in Fig. 3 corresponds to a somewhat higher cooling rate ($\dot{T} \sim 10^6$K/sec) than that assumed in the ΔH_m-r/R plot, Fig. 2 (which may correspond to $\dot{T} \sim 10^5$K/sec); if the 10^6K/sec contour were drawn on the ΔH_m-r/R plot, it would enclose at least the Zr-Cr point also. Alternative suggestions to explain such discrepancies can be based on the origin of the data used in the ΔH_m-r/R plots, discussed below.

Use of T-C plots can be extended to alloys other than eutectics in terms of their reduced liquidus point differences and their reduced compositions. This introduces some needs for a redefinition of the reduced parameters, discussed in more detail in Ref. 13. Thus, in the hypereutectoid composition range as well as between two intermetallic phases, the reduced composition difference is generally = 1.0. This is so because the alloy composition is measured with respect to the composition of the competing intermetallic phase; however, intermediate phases in RGF metal-metal alloy systems rarely have extended solid solution ranges, i.e., the reduced parameter $C_r = (C - C_{sol.sol.})/(C - C_{cpd}) \neq 1$, if $C_{sol.sol.} \neq C_{pd}$. With such suitable extension of the parameters, however, T-C maps can be used to account for the composition range of RGF in a given system; details are discussed in Ref. 13.

ORIGIN AND INTERRELATION OF THE PARAMETERS USED

The parameters used in both types of plots are functions of the alloy system. This is true of ΔH_m and r/R as well as for the phase diagram features used in the T-C map. At present, the parameters in both types of plots are not amenable to *ab initio* calculations from elemental parameters for most systems of interest; this is a result of the complexity of the interactions and phase diagrams involved in RGF systems.

However, a practical difference between both types of diagram is that the parameters for the T-C plot are readily accessible if the phase diagram is known, while at least one of the ΔH_m-r/R plot parameters, ΔH_m, requires a

rather difficult measurement. By contrast, there exists a simple, semi-empirical approach to obtaining ΔH_m from elemental quantities, namely Miedema's theory [14] which provides a relation of ΔH_m to the elemental electronegativities χ and the electron concentrations (each of these parameters contains, implicitly or explicitly, the atomic volume and, hence, atomic size). The ΔH_m-r/R plots thus allow the prediction of RGF from elemental parameters. The ΔH_m values used in Figs. 1 and 2 have been derived in this way. It should be mentioned that despite the frequently good agreement of Miedema theory values with experiment, [14] the theoretical foundations of this theory are not secure and form the subject of discussion. [15]

The atomic size ratio, r/R, used in the ΔH_m-r/R plots is also an unsatisfactory parameter. While it can be computed unambiguously from elemental data, the relevance of this computed quantity to binary alloys is not clear. Crystal structure studies show that the atomic sizes of the components (i.e., appropriately partitioned interatomic distances in the solid) are quite different for different and like neighbors and, further, vary strongly with composition over the diagram; hence, the elemental r/R values are quite unrepresentative of the actual atomic sizes in the alloys. As an example, the variations of interatomic spacings with composition are shown for the two intermetallics in the RGF system Mg-Cu in Fig. 4 of Ref. 11. It appears that the change of size of an atom in an alloy is related *inter alia* to the binding energy and hence to ΔH_m; however, the quantitative form of this connection is not known. Further, the component size ratio plays a role in ΔH_m, as shown, e.g., for interalkali alloys. [16]

It should be mentioned that the plots introduced by Alonso-Simozar [17] to predict solid solubility use essentially the same parameters as the ΔH_m-r/R RGF plots; the two types of diagrams are complementary in that they span different regions of the plot for solid solubility and RGF.

Addressing the relation between the ΔH_m-r/R and the T-C plots presented, we note that the parameters of both plots are highly correlated; the phenomenological parameters of the T-C plot are functions of ΔH_m and r/R. Thus, the maximum solid solution range of the T-C plot is related directly to r/R via the Hume-Rothery rule [18] and, on a deeper level, to the combination of ΔH_m and r/R via the Alonso-Simozar plot. [17] The eutectic melting point depression T_{er} is a function of the non-ideality of the solution, which is related to ΔH_m where the latter is also related to r/R as noted above. Given these relationships, the predictions from both diagrams should therefore agree if properly formulated.

Last, we turn to the reason for the observed correlations between the parameters in our diagrams and RGF; i.e., we ask why "it works." According to the kinetic theory of glass formation, RGF occurs if the melt viscosity at the liquidus temperature is high; this is related to a high value of the reduced glass transition temperature, $T_{gr} = T_g/T_L$. [2] Starting with the ΔH_m-r/R plot, both a large ΔH_m and a small r/R should increase the melt viscosity: increasing ΔH_m is associated with increasing the short range order and hence, increasing the energy of the "wrong-nearest-neighbor" barrier that must be overcome during atomic rearrangement; a small r/R acts in the same direction, possibly by providing more efficient space filling and decreasing the available free volume.

As to the T-C map, the T parameter acts directly on T_{gr} which increases as T_L is decreased. Further, the C parameter reflects the elimination of alternative, simple crystallization paths into a metastable, extended terminal solid solution. [19] Each parameter involved in either plot thus affects the RGF appropriately.

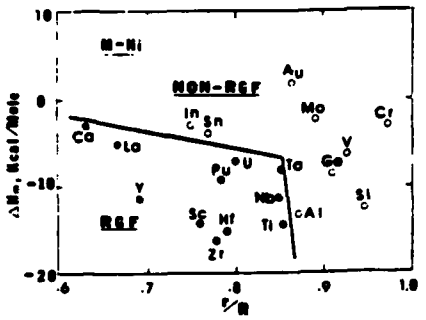

Fig. 1. The ΔH_m-r/R RGF plot for binary alloy systems containing Ni. [5,11] Systems with RGF and non-RGF are indicated by closed and open circles, resp.

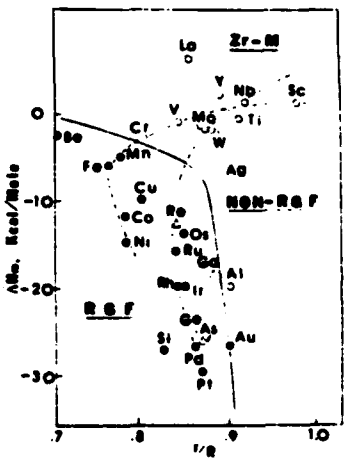

Fig. 2. The ΔH_m-r/R RGF plot for binary alloy systems containing Zr. [11] Systems not tested given by triangles. Dashed lines trace out first long period and second/third long period addition elements.

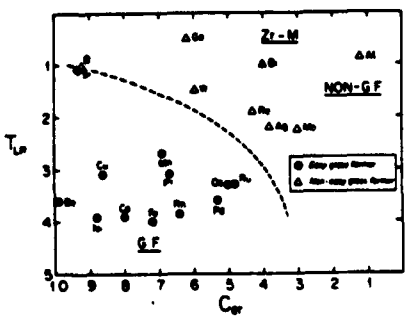

Fig. 3. The reduced temperature-reduced composition (T-C) RGF maps for the terminal, Zr-rich eutectics of the Zr-M systems shown. Systems with easy glass formation (RGF) and non-easy glass formation (non-RGF) given by closed circles and triangles, resp.

ACKNOWLEDGMENT

The authors are grateful for initial support of this work by the National Science Foundation and further support by the U. S. Army Research Office. One of us (SHW) wishes to acknowledge support by the Office of Naval Research. We are also pleased to acknowledge suggestions from Dr. C. L. Tsai.

REFERENCES

1. W. Klement, Jr., R.H. Willens, and P. Duwez, Nature 187, 869 (1960).
2. D. Turnbull, J. Phys. (Paris) 35, Colloque C-4, C4-1 (1974).
3. D.E. Polk and B.C. Giessen, in: Metallic Glasses, J.J. Gilman and J.H. Leamy, eds. (ASM, Metals Park, OH 1978), p. 1.
4. S. Takayama, J. Mater. Sci. 11, 164 (1976).
5. B.C. Giessen and S. Whang, J. Phys. (Paris) 41, Colloque C-8, C8-95 (1980).
6. B.C. Giessen and D.E. Polk, in: Theory of Alloy Phase Formation, L.H. Bennett, ed. (TMS-AIME, Warrendale, PA 1980), p. 487.
7. J. Hafner, Phys. Rev. B21, 406 (1980).
8. H. Jones, Rep. Prog. Phys. 36, 1425 (1973).
9. L.S. Darken and R.W. Gurry, Physical Chemistry of Metals (McGraw-Hill, New York 1953), p. 74.
10. L.H. Bennett and R.E. Watson, in: Theory of Alloy Phase Formation, L.H. Bennett, ed. (TMS-AIME, Warrendale, PA 1980), p. 390.
11. B.C. Giessen, in: Proc. Fourth Internat. Conf. on Rapidly Quenched Metals, Vol. I, T. Masumoto and K. Suzuki, eds. (The Japan Institute of Metals, Sendai 1981), p. 213.
12. A. Inoue, Y. Takahashi, N. Toyota, T. Fukase and T. Masumoto, in: Proc. Fourth Internat. Conf. on Rapidly Quenched Metals, Vol II, T. Masumoto and K. Suzuki, eds. (The Japan Institute of Metals, Sendai 1981), p. 1221.
13. S.H. Whang, Mater. Sci. and Eng. 57, 87 (1983).
14. A.R. Miedema and P.F. de Châtel, in: Theory of Alloy Phase Formation, L.H. Bennett, ed. (TMS-AIME, Warrendale, PA 1980), p. 344.
15. C.H. Hodges, in: Theory of Alloy Phase Formation, L.H. Bennett, ed. (TMS-AIME, Warrendale, PA 1980), p. 503.
16. J. Hafner, Private Communication.
17. J.A. Alonso and S. Simozar, Phys. Rev. B22, 5583 (1980).
18. W. Hume-Rothery, J. Inst. Met. 35, 295, 307 (1926).
19. W.J. Boettinger, in: Rapidly Solidified Amorphous and Crystalline Alloys, MRS Symp. Proc. Vol. 8, B.H. Kear, B.C. Giessen, and M. Cohen, eds. (North Holland, NY 1982), p. 15.

CRYSTALLIZATION BEHAVIOR OF BINARY METALLIC GLASSES CONTAINING Pt

Y. Q. Gao and S. H. Whang

Northeastern University
Boston, MA 02115

CRYSTALLIZATION BEHAVIOR OF BINARY METALLIC GLASSES CONTAINING Pt

Yi Qun GAO and Sung H. WHANG

Barnett Institute of Chemical Analysis & Materials Science, Northeastern University, Boston, MA 02115

Binary M-Pt glasses were made by rapid quenching from liquid, where M is Ti, Zr, and Hf. Glass forming compositions were found near eutectics in Ti-Pt, Zr-Pt and Hf-Pt. Isothermal crystallization for $Zr_{75}Pt_{25}$ was studied at a temperature range from 780 to 792°K. The non-isothermal transformation was measured by differential scanning calorimetry with heating rates from 5 to 160 K/min. Activation energy for crystallization was obtained from the non-isothermal heating, which is consistent with that from the isothermal annealing.

1. INTRODUCTION

Since many metallic glasses have been synthesized *via* rapid solidification, the crystallization behavior of these glasses has become the subject of interest for scientists and engineers.

Previously, only a few binary Pt containing glasses were reported either because expensive materials costs discouraged active research in these areas or because Pt alloys are not good glass formers. Some of these glassy alloys reported are Ti rich Ti-Pt and Zr rich Zr-Pt compositions[1,2] in which the crystallization properties are not known.

Although crystallization of ternary Pt glasses, Pt-Ni-P was studied before,[3] binary Pt-transition metal glasses are expected to show different crystallization behavior from that of the Pt glass containing P.

2. EXPERIMENTAL

Small Pt alloy buttons were made from pure Pt, Ti, Zr, and Hf (all 99.9%) in an arc melting furnace and subsequently were splat-quenched into foils using the hammer and anvil technique. Amorphousness was judged from a broad diffraction peak in x-ray pattern. Both isothermal and non-isothermal annealing were carried out by differential scanning calorimetry (DSC). For isothermal annealing, the sample was heated up at a rate of 320 K/min to the desired annealing temperature while non-isothermal tests were conducted with heating rates of 5, 10, 20, 40, 80, and 160 K/min.

The effective annealing time was calculated by subtracting the incubation time for crystallization from the total annealing time. The incubation time was determined from the intersecting point of the DSC trace and the base line near the starting point.

3. RESULTS

3.1. Glass Forming Ability

There are two favorable conditions for glass forming in binary Pt-Group IVB (Ti, Zr, Hf); one is atomic size ratio, and the other is large electronegativity differences between the two component atoms.[4] Beyond these immediate indications, the binary Pt phase diagrams that consist of a relatively deep eutectic combined with a low solid solubility near the Group IVB rich side constitutes an easy glass forming criterion.[2]

The glass forming compositional ranges are shown in Fig. 1. Glass forming ranges in Zr-Pt and Hf-Pt are similar to each other and larger than that in Ti-Pt. By contrast, at the Pt rich side, as-quenched $Pt_{99.5}Zr_{.5}$ turned out to be crystalline.

3.2. Crystallization Kinetics

3.2.1. Isothermal Transformation

If the nucleation rate and growth rate are constant at a given temperature, the fraction transformed, x can be expressed by the relation

$$x(t) = 1-\exp(-k\ t_e^{\,n}) \tag{1}$$

where t_e is effective annealing time which excludes incubation time, and n is a constant called transformation mode parameter. This relation is known as Johnson-Mehl-Avrami equation.[5] In order to obtain the transformation rate, take the derivative of x with respect to t_e

$$\frac{dx}{dt_e} = K\cdot n\cdot t_e^{n-1}\exp(-Kt_e^{n}) \tag{2}$$

Now, the maximum rate occurs at $\frac{d^2x}{dt_e^2} = 0$ in a DSC isothermal pattern, in which $t_e = t_e(\max)$ and

$$t_e(\max) = \left(\frac{1}{K}\right)^{\frac{1}{n}} \left(\frac{n-1}{n}\right)^{\frac{1}{n}} \tag{3}$$

by substituting (3) into equation (2), the maximum transformation rate, $\left(\frac{dx}{dt}\right)_p$ is

$$\left(\frac{dx}{dt}\right)_p = K^{\frac{1}{n}} n^{\frac{1}{n}} (n-1)^{\frac{n-1}{n}} \exp\left(-\frac{n-1}{n}\right) = C_1 K^{\frac{1}{n}} \tag{4}$$

where C_1 is a constant. Therefore, the fraction transformed at $t_e(\max)$, x_p is

$$x_p = 1 - \exp\left(-\frac{n-1}{n}\right) \tag{5}$$

Finally, the activation energy for the isothermal transformation is determined from Eq. (4) and an Arrhenius type equation since $T<T_m$ and $\Delta E>>RT$ in metallic glasses, *i.e.*, $K' = K_0' \exp\left(-\frac{\Delta E}{RT}\right)$, where K' is $K^{1/n}$ and only a function of T. Therefore, $\Delta E/R$ can be obtained from a slope in a plot of $\log\left(\frac{dx}{dt}\right)_p$ and $1/T$.

Fig. 2 shows a typical isothermal thermogram obtained by DSC. The area

encircled by the base line and the DSC trace was divided into from 60 to 80 sections and was calculated using a computer. The fraction crystallized was assumed to be proportional to the fraction of the area.

alloy composition	y = 10	20	30	40	50
$Ti_{100-y}Pt_y$		x	x x o o	x	
$Zr_{100-y}Pt_y$		x	o o o	o	x
$Hf_{100-y}Pt_y$		x	o o o	o o	x

o glass, x crystalline

Figure 1
glass forming composition

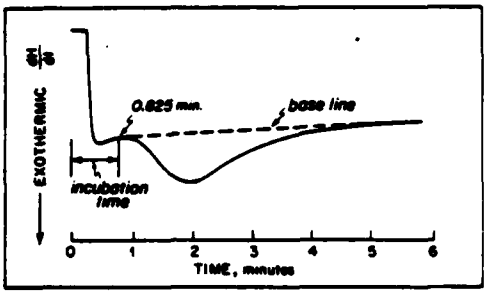

Figure 2
DSC trace for the isothermal crystallization of $Zr_{75}Pt_{25}$ glass at 788K

i.e., $\frac{dH}{dt} \alpha \frac{dx}{dt}$ and the normalization condition $\int_0^\infty (\frac{dx}{dt})dt = 1$.[6,7] To apply this isothermal method to $Zr_{75}Pt_{25}$alloy, we carefully investigated a possible overlap between the first crystallization reaction and the second exotherm since two different exotherms in the DSC trace of a continuous heating with 80K/min. were found at 858K and 934K as peak temperatures. Specimens were annealed isothermally at 788K, 820K, 860K, and 880K respectively after heating each sample to the isothermal annealing temperature with a heating rate of 320K/min. The results show that: at 788K, the first crystallization exotherm appears alone; at 820K, still the first exotherm is the only reaction within 30 mins.; at 860K, both the first and the second exotherms show up with a high intensity. The first crystallization nearly ends at 1 1/2 mins. and the peak intensity of the second exotherm exists at 6 1/2 mins. No overlap was observed between the two reactions; finally, at 880K, the first exotherm almost diminishes and the strong second exotherm is observed. From this series of experiment, it is confirmed that the second reaction doesn't appear at 788K within a reasonable time and, therefore, no overlap of the two reactions can be identified experimentally at this temperature. Also, the heat of evolution for the first reaction is estimated to be seven times larger than that of the second exotherm, which is determined from the non-isothermal scanning (a heating rate of 160K/min.). All these facts indicate that in the isothermal annealing at 788K the first crystallization reaction can be safely isolated without the interference of the second reaction. Isothermal crystallization of $Zr_{75}Pt_{25}$ glass as a function of annealing time was plotted in Fig. 3. In order to obtain n value, using Eq. (1) $\log[\log(\frac{1}{1-x})]$ was plotted against $\log t_e$ as shown in Fig. 4. The slopes are fairly straight for the range of $0.04 \leq x < 0.9$ and yield n values of 2.6 ± 0.2. These values are consistent with those obtained from Eq. (5) in

which x_p was determined experimentally. The n values by Eq. (5) are listed in Table 1.

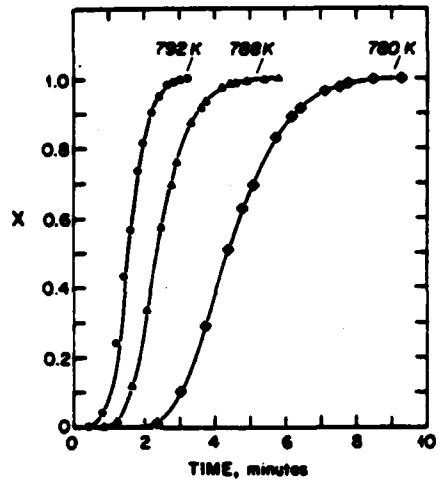

Figure 3
fraction of crystallization, x versus total annealing time, t in $Zr_{75}Pt_{25}$

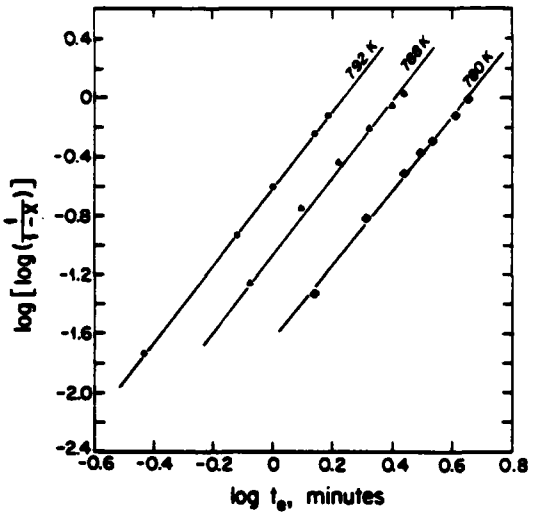

Figure 4
$\log[\log(\frac{1}{1-x})]$ versus $\log t_e$ for $Zr_{75}Pt_{25}$ glass

Temperature T(k)	x_p	n
780	0.43	2.3
788	0.44	2.4
792	0.44	2.4

TABLE 1: n values for various temperatures in $Zr_{75}Pt_{25}$

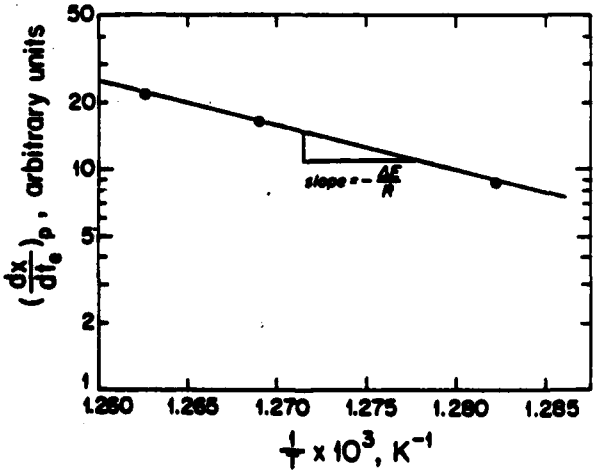

Figure 5
maximum crystallization rate $\log(\frac{dx}{dt})_p$ versus 1/T for $Zr_{75}Pt_{25}$ glass

On the other hand, the activation energy can be found in a plot of $\log (\frac{dx}{dt})_p$ vs. 1/T as discussed above. The activation energy determined from Fig. 5 is 81 K cal/mol.

3.2.2. Non-Isothermal Transformation

Differential scanning techniques provide many advantages over isothermal annealing, and therefore cannot be overlooked. Despite such merits, the theoretical foundation of this approach has not been well established since nucleation and growth rates change as a function of temperature. An elegant mathematical method dealing with these complicated problems is not available. We will take the empirical approach proposed by Kissinger,[8]

$$-\frac{\Delta E}{R} = \frac{d \ln \left(\frac{\beta}{T_p^2}\right)}{d\left(\frac{1}{T_p}\right)} \qquad (6)$$

where T_p is the temperature at which the maximum transformation rate occurs and β is heating rate. The Kissinger equation may be expanded as

$$-\frac{\Delta E}{R} = 2T_p + \frac{d(\ln\beta)}{d\left(\frac{1}{T_p}\right)} \approx \frac{d(\ln\beta)}{d\left(\frac{1}{T_p}\right)} \qquad (7)$$

If $2T_p$ is small relative to the other term, Eq. (7) is a useful approximation. In fact, the resulting activation energy by this approximation is 2-4% larger in terms of absolute magnitude[9] than that calculated by the Kissinger equation. Crystallization temperatures for $Ti_{65}Pt_{35}$, $Zr_{75}Pt_{25}$ and $Hf_{75}Pt_{25}$ glasses are shown in Table 2. The relevant activation energies also are listed at the bottom of the Table.

β	alloy	$Ti_{65}Pt_{35}$		$Zr_{75}Pt_{25}$			$Hf_{75}Pt_{25}$	
	$T_{e(K)}$	T_{p_1}	T_{p_2}	T_x	T_{p_1}	T_{p_2}	T_x	T_{p_1}
5(K/min)		808	927	805	813	886	919	928
10		818	945	811	823	896	934	941
20		835	963	821	833	909	943	955
40		854	977	830	844	919	962	972
80		870	997	842	858	934	---	---
160		---	---	859	878	953	---	---
ΔE (kcal/mol)		61.7	76.0	82.5	77.6	91.7	86.7	86.7

T_x: onset temperature ΔE: activation energy
T_{p_1}: first peak temperature T_{p_2}: second peak temperature

TABLE 2: Crystallization temperature and calculated activation energy

4. DISCUSSION

The relatively poor glass forming ability of Ti-Pt comes from the fact that the small atomic size difference between Ti and Pt stabilizes the solid solution against the glassy phase. Also, the similarity of glass forming tendency

between Zr-Pt and Hf-Pt may be due to the resemblance to each other in atomic size and electron configuration. In particular, a wide glass forming range in Zr-Pt is impressive because the liquidus line between 33 and 45 at % Pt which is confined by two compounds, *i.e.*, Pt Zr and Pt Zr_2 lies above the ideal liquidus line. However, it appears that the nucleation and growth of Pt Zr and Pt Zr_2 are slow and no other metastable phase is available except glass phase at this cooling rate. Details are discussed elsewhere.[10]

The n value obtained from isothermal experiment is close to 3.0 which is known to be eutectoid-type reaction with a constant growth rate.[5] This value could vary significantly depending upon thermal history as indicated in a recent report.[11] However, the confirmation of the mechanism should wait until the microstructural study by TEM is completed.

There exists a systematic correlation among crystallization temperature, activation energy and weighted average of the melting temperature as shown in Table 3.

alloy	T_{p_1}(K) (β=10K/min)	ΔE(kcal/mol)	weighted ave. melting temperature (K)
$Ti_{65}Pt_{35}$	808	61.7	1976
$Zr_{75}Pt_{25}$	813	77.6	2103
$Hf_{75}Pt_{25}$	928	86.7	2382

TABLE 3

In other words, with increasing ideal melting temperature, crystallization temperature as well as activation energy increases.

6. CONCLUSION

1. Glass forming compositions were identified in all binary Group IVB-Pt systems. Relatively wide glass forming occurs in Zr-Pt and Hf-Pt.

2. Transformation mode parameter, n for $Zr_{75}Pt_{25}$ was found to be 2.55 $\pm$ 0.25.

3. High crystallization temperatures were discovered in all the binary systems. The temperatures vary from 808 to 972 K for the first crystallization. The relevant activation energies change from 62 to 87 Kcal/mol.

4. A correlation exists among crystallization temperature, activation energy and weighted average of melting temperatures.

ACKNOWLEDGEMENT

We thank Prof. B.C. Giessen for his encouragement and advice. One of us (SHW) wishes to express his appreciation for financial support by the Office of Naval Research, VA (Grant No. N00014-82-K-0597). Contribution #179 of Barnett Institute of Chemical Analysis and Materials Science.

REFERENCES

1) B.C. Giessen and S.H. Whang, Journal de Physique, Colloque C8 (1980) 95.

2) S.H. Whang, Mat. Sci. Eng. 57 (1983) 87.

3) H.S. Chen, Acta Met. 22 (1974) 1505.

4) D.E. Polk and B.C. Giessen, in "Metallic Glasses", ASM, 1976.

5) J.W. Christian, The Theory of Transformation in Metals and Alloys, 2nd Ed. (Pergamon Press) (1975) 540.

6) H.J. Borchard and F. Daniels, J. Am. Chem. So. 78 (1957) 41.

7) D.W. Henderson, J. Non-Cryst. Sol. 30 (1979) 301.

8) H.E. Kissinger, Anal. Chem. 29 (1957) 1702.

9) Y.Q. Gao, et al., Proc. 4th Int. Conf. RQM, Sendai, Japan (1981) 727.

10) S.H. Whang, Proc. Int. Conf. Liquid & Amorphous Metals, Aug., 1983, UCLA, CA, J. Non-Cryst. Sol. (Special Issue).

11) P.G. Boswell, J. Mat. Sci. 15 (1980) 1939.

MECHANICAL CHOPPER FOR RAPIDLY QUENCHED METALLIC RIBBON

S. H. Whang and B. C. Giessen

Northeastern University
Boston, MA 02115

P/M FLAKE MATERIAL PREPARED BY MECHANICAL CHOPPING OF RAPIDLY QUENCHED METALLIC RIBBON

S.H. Whang and B.C. Giessen

Materials Science Division
Barnett Institute of Chemical Analysis & Materials Science

Northeastern University
Boston, MA 02115

Abstract

Ductile metallic ribbons prepared by melt spinning can be easily cut into flakes suitable for P/M processing by a mechanical chopper designed to tear off ribbon flakes by combining a rotating blade and a bed knife. Details of the design features are described.

INTRODUCTION

Alloys rapidly quenched as melt spun ribbons have superior cooling rates and uniformity compared to alloys atomized as powder; however, wide application of ribbon processes to make bulk alloys by P/M has been hampered by the fact that thin ribbons are not well suited to direct compaction and subsequent P/M consolidation. To obtain powders from ribbons, pulverization e.g., by hammer milling, can be used for brittle ribbons; alternatively, certain ductile ribbons can be pulverized following reversible hydrogen embrittlement (1). However, most quenched alloy ribbons of current technical interest are neither brittle nor can they be treated easily by hydrogen embrittlement. As an alternative, we have examined the possibility of chopping the ribbon mechanically into flakes which can be used for P/M processing.

DESIGN FEATURES

Figure 1 shows a schematic drawing of a chopper designed to tear off melt spun alloy ribbon at various speeds into pieces of various lengths. The chopper consists essentially of feeding components and chopping components. Ribbons are fed in by one or two coupled rollers that supply the ribbon to the chopper at a constant rate. The chopping components include a bed knife and a roller with two tungsten carbide blades. The two components are driven separately by two motors. The length of the chopped ribbon pieces L is determined by the ratio of the feeding speed and the cutting speed,

$$L = \frac{D \cdot M}{I \cdot N}, \qquad (1)$$

M: rotation rate of the feeding roller,

N: rotation rate of the cutting roller,

D: diameter of the feeding roller,

I: number of blades on the cutting roller.

In order to reduce L significantly, I or N must be increased, assuming a constant feeding speed, which is determined by the melt spinning process taking place prior to chopping.

Details of the chopping component are shown in Figures 1 and 2. The rotating blades, tilted at an angle of 15^0 against the bed knife, initiate a crack at the edge of the ribbon and then tear it off in a shearing motion. This characteristic of the process is essential; once the crack is generated, its propagation across the ribbon width requires only a small amount of tearing force. By contrast, a cut in which the rotating blade is parallel to the bed knife and moves normal to it would require considerable force. For example, in amorphous metals, the crack extension force F_c at which catastrophic tearing occurs (2)(3) is:

$$F_c = (\sigma_y . \varepsilon_f) . t \qquad (2)$$

where σ_y is yield stress, ε_f is strain to failure and t is the ribbon thickness. If the sheet is ∿2mm wide, ∿25μm thick, ε_f is ∿1.5×10^{-5} and σ_y is taken to be ∿6 GPa, F_c ∿2.25 Pa according to equation (2). By contrast, if similar assumptions are made for a normal cut with parallel knife edges, F_c increases to ∿180 Pa. Thus, in this case, the ribbon may readily bend into the gap between the blade and the bed knife instead of being cut.

Result: Using a cutter with I=2 and D∿150mm and operating conditions of M=14 and N=1050, 1 mm wide ribbons of highly ductile CuZr metallic glass were readily cut into 1 mm long flakes of approximately square shape suitable for compaction e.g., by hot extrusion. In order to improve the capability of the equipment, especially the cutting rate, use of highly wear-resistant materials for the blade and the bed knife is essential.

ACKNOWLEDGEMENT

This unit is part of the DARPA sponsored melt spinning facility at Northeastern University; one of us (SHW) thanks for support by the Office of the Naval Research, and the other (BCG) acknowledges support by the Army Research Office Durham.

Contribution #182 of the Barnett Institute.

REFERENCES

1. B.C. Giessen, S.H. Whang and F. Dabkowski, in Rapid Solidification Processing III, Ed. R. Mehrabian, 1983, NBS, Washington, D.C., p. 435.
2. R.S. Rivlin and A.G. Thomas, J. Polymer Sci. 10 (1952) 291.
3. H. Kimura and T. Masumoto, Scripta Met. 9 (1975) 211.

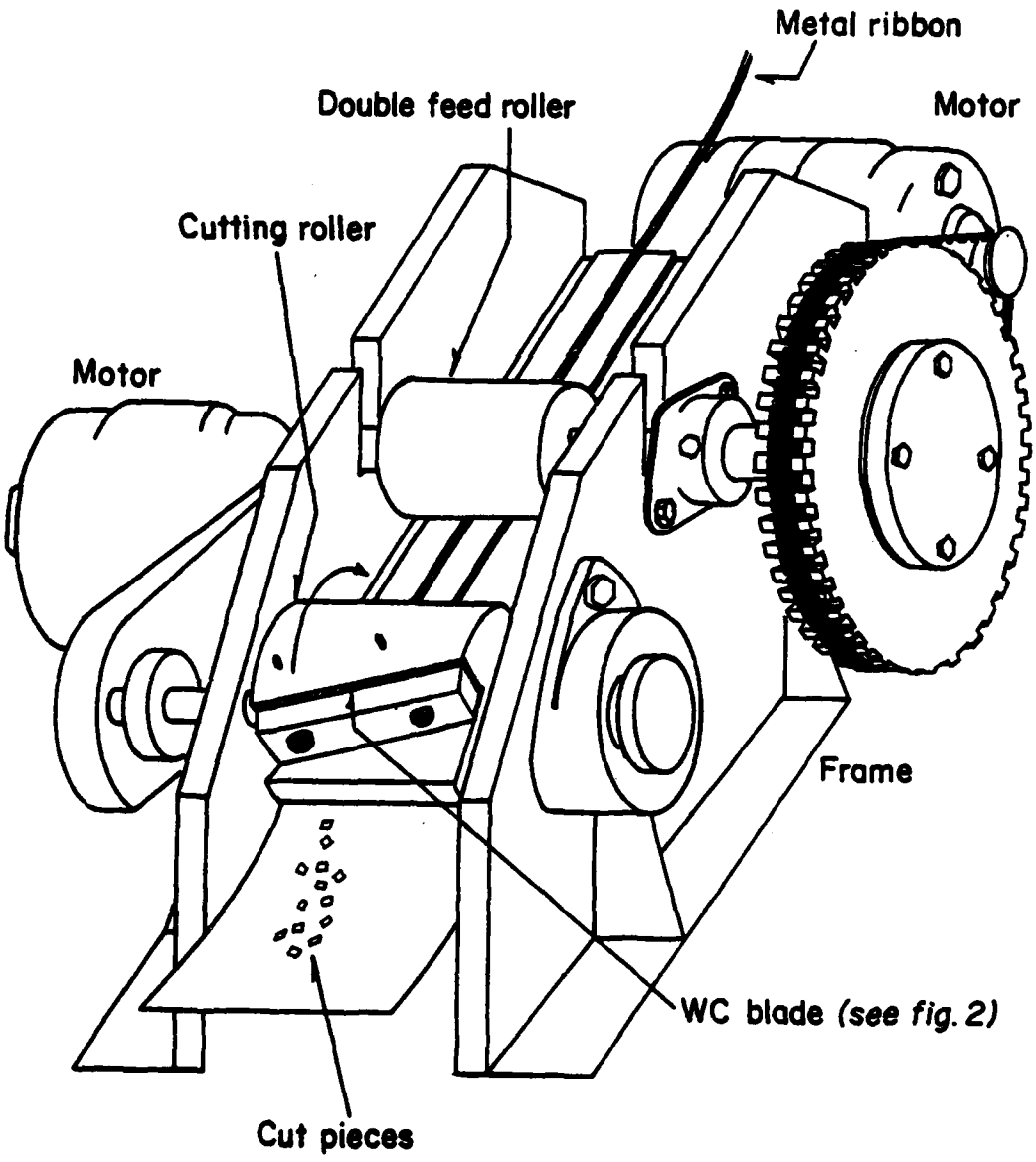

FIGURE 1

Schematic drawing of high speed chopper for preparation of melt spun ribbon flakes

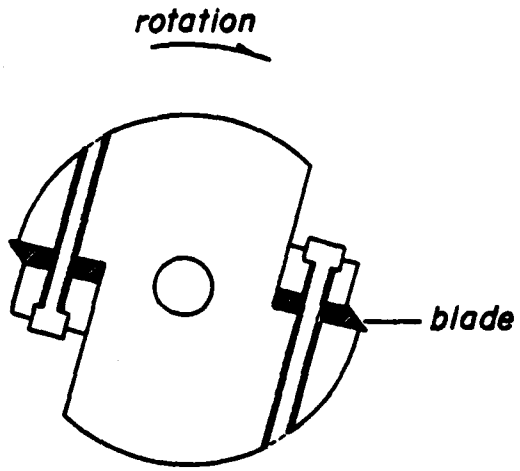

Cross-section of cutting roller

FIGURE 2

Detail drawing of cutting roller

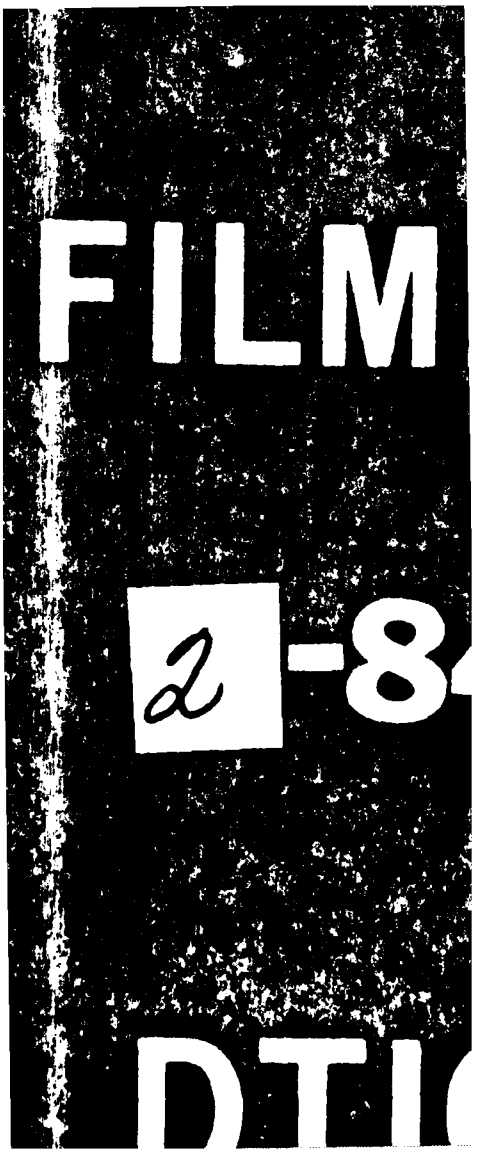
FILM
2-8
DTI